ELSEVIER

Contents lists available at ScienceDirect

# Construction and Building Materials

journal homepage: www.elsevier.com/locate/conbuildmat





# Enhancing carbonation and strength of MgO cement through 3D printing

AlaEddin Douba\*, Palash Badjatya, Shiho Kawashima

Columbia University, Department of Civil Engineering and Engineering Mechanics, 500 West 120th Street, New York, NY 10027, USA

ARTICLE INFO

Keywords:
Magnesium Oxide (MgO) cement
3D concrete printing
Rheology
Carbon sequestration
Carbon capture and storage

### ABSTRACT

Magnesium oxide (MgO), which develops physical strength through carbonation, is a potential alternative to carbon intensive Portland cement. In this paper, we examined whether 3D printing could improve carbonation and compressive strength. The rheology of MgO paste was modified using mixtures of nanoclays and methyl-cellulose to produce cylinders with exposed open-to-air and closed (solid) infills. The results showed significant increases in strength at 3 and 28 days compared to conventionally cast specimens. This was attributed to higher exposed surface area and increase in porosity caused by high early water evaporation, both of which led to higher CO<sub>2</sub> intake.

### 1. Introduction

There has been significant interest in using carbon capture and storage technologies to reduce atmospheric carbon dioxide [1]. Carbon dioxide sequestration in construction is gaining traction as well [2] especially since concrete is the most widely used material in the world, second only to water. The main ingredient in concrete today is Portland cement and given the scale of use, its manufacture accounts for 7-8 % of global greenhouse gas emissions [3]. Global cement production was 4.1 billion metric tons in 2019 [4], and is projected to grow by 12 % by 2050 [5]. One important step in improving construction sustainability is by introducing alternative lower carbon emission binders that can help replace or supplement Portland cement use [6]. Slag and fly ash, which are by-products of different industries, are widely used cement alternatives. However, quality control limitations, low replacement levels, and potential decrease in early age strength [7] may deter from making sustainable environmental impact. Alkali-activated materials, geopolymers and calcined clay cements are some other alternatives that have been explored [8-11], but have not realized momentous uptake by

Magnesium-based cements have been identified as another alternative due to abundance of magnesium on earth, especially in oceans [12,13]. Magnesium oxide (MgO) in particular has been used in construction in the past in the form of magnesium oxychloride, magnesium phosphate, and magnesium oxysulfate for non-structural applications like fire protection and insulation [14]. MgO has also been used as an additive to overcome shrinkage [15] due to expansion caused by its conversion to Mg(OH) $_2$  (brucite) in the hydrating system. Because

brucite has lower mechanical strength, the use of MgO as the primary binding material or even as a significant replacement of Portland cement has been limited. However, the true appeal of MgO is that it can react with CO<sub>2</sub> to produce various magnesium carbonates such as nesquehonite (MgCO<sub>3</sub>·3H<sub>2</sub>O), hydromagnesite (4MgCO<sub>3</sub>·Mg(OH)<sub>2</sub>·4H<sub>2</sub>O), or dypingite (4MgCO<sub>3</sub>·Mg(OH)<sub>2</sub>·5H<sub>2</sub>O) which lend themselves to strength, while also acting as carbon sinks [2]. There are however some challenges associated with using MgO for construction: carbonation at ambient conditions is a slow process leading to slow strength development [12]. Additionally, CO2 intake decreases as magnesium carbonates begin to form inside the exposed exterior walls that slows and eventually prevents carbon penetration. For example, up to 55 % uncarbonated brucite (hydrated MgO) has been found in cylindrical MgO-based concrete specimens [16,17] disallowing the binding matrix from reaching its maximum strength. However, because 3D printing enables complexity free of cost, it allows for the creation of elements with higher surface area to volume ratio that could potentially facilitate greater CO<sub>2</sub> delivery and intake which subsequently leads to improved strength.

Rheological properties and printing parameters are highly linked and their interdependency correlates to the mechanical performance. The ever-changing rheological and hydration properties of Portland cement result in continuously altered printing process parameters and in turn cause variations in wet and dry properties and performance of 3D printed elements [18–22]. For example, Wolfs and Salet utilized their findings alongside that of Panda et al. [23] to indicate that the nozzle height impact on print geometry and, in turn, on mechanical performance is dependent on the initial static yield stress and structuration rate [24]. Nevertheless, the effects of static yield stress, elastic modulus,

E-mail address: ad3456@columbia.edu (A. Douba).

<sup>\*</sup> Corresponding author.

structuration rate, and viscosity on printing properties have been well documented [25–32]. Printing paths play a critical role in determining interfilamentous and interlayer bond strengths [33,34] for 3D printed concrete which can lead to anisotropic mechanical properties [18,20,21,30–33,35–38]. However, the dependency on print path is in turn dependent on the mixture properties, as researchers have reported both lower [24,33,36] and higher [34,39] compressive strengths of elements tested perpendicular to layer height. 3D printed MgO is novel and has only been reported by Khalil et al. who showed an increase in compressive strength from 18 to 30 MPa due to 3D printing [40]. The effects of printing patterns and anisotropy of the prints of MgO are unknown but can be expected to display similar performance to Portland cement.

Studies have shown that conventional Portland cement can become 3D printable using thixotropic admixtures, alternative binders and accelerators [23,24,35–39,41,42,32,33,43–47]. Adopting a similar approach of adding admixtures to MgO binders, accelerated hydration for MgO can be achieved using magnesium acetates [48,49] or brucite [50]. With the aid of polycarboxylate ether, hydroxyethyl cellulose and defoamer, Khalil et al. [40] were able to make a 3D printable MgO paste. On the other hand, replacement of MgO with compatible alternative binders can potentially reduce the environmental benefit of MgO concrete as less carbonation has been observed when MgO was partially replaced by ground granulated blastfurnace slag (GGBS) or brucite [50]. Lastly, the rheology of MgO concrete and its compatibility with thixotropic additives has not been well studied [51]. In Portland cement systems, nanoclays (NCs) have been reported by many authors to offer significant increase in static yield stress compared to viscosity and have been widely adopted for concrete 3D printing [32,52–58].

Previous work by Douba et al [59] has shown that the thixotropic behavior of NC-modified Portland cement is driven by colloidal interactions due to adsorbed ions, electrostatic attractions and van der Waals forces rather than by chemical bonds associated with cement hydration products such as calcium silicate hydrates (C-S-H). Thus, NCs have high potential in showing similar thixotropic benefits in MgO cement systems despite the differences in hydration kinetics and products between the two binders. NCs have also been coupled with polymeric viscosity modifying admixtures (VMAs) to meet the rheological demand of 3D printing [32,43–46,60]. The high water adsorption associated with NCs [61], which can produce stiff filaments [53] causing tearing or splitting, can be compensated by the increase in viscosity due to VMAs, which is associated with an increase in filament cohesion [44,62] as well as increased stability [40,63].

In this work, the effects of NCs and methylcellulose (MC) as rheological modifiers were studied first, where the combination of NC and MC in MgO paste has been investigated here for the first time, by measuring static yield stress, dynamic viscosity and macroscopic elastic modulus. Two mixtures with different water/binder (w/b) ratios and suitable rheological properties were then selected to test the efficacy of 3D printing in increasing carbon penetration and intake. Cylinders with 25.4 mm diameter and height were 3D printed using exposed open-to-air and closed (solid) infills and their compressive strengths at 3 and 28 days of carbon curing were compared with those of conventionally cast cylinders with the same dimensions. Thus, the mechanical investigation examined the effects of rheological modifiers, w/b ratio, and printed infill pattern on compressive strength gain, which is still highly underinvestigated for MgO cement systems. To the authors' knowledge, this is the first peer-reviewed study investigating the rheology and effects of different infill patterns at similar load-orientation of MgO paste modified with NC and MC. Additionally, chemical characterization using XRD and TGA was conducted to study the effect of carbonation curing by comparing the phase assemblage between carbonated and uncarbonated specimens.

### 2. Experimental program

### 2.1. Materials

A high reactivity light burned magnesium oxide powder with  $>98\,\%$  purity was obtained from Martin Marietta Magnesia Specialties with commercial name MagChem-30 and used for this study. The chemical composition and physical properties are shown in Table 1. The nanoclays used were homogeneously shaped palygorskite or attapulgite nanorods with length of 1.5–2.0  $\mu m$  and diameter of 30 nm, supplied by Active Minerals under the commercial name Acti-Gel 208. The VMA used was a low molecular weight methylcellulose (MC) polymer with molecular weight of 14,000 and a degree of substitution of 1.5–1.9, supplied by Millipore Sigma. Both NC and MC were used by addition rather than substitution to MgO by weight of MgO powder.

## 2.2. Specimen preparation

The high specific surface area of MgO requires significantly higher w/b ratio than what is typically used for Portland cement. The rheology of plain MgO paste was characterized for w/b ratios of 1.1 and 0.9 as they represented the highest and lowest workable water contents respectively to produce mixable paste with no segregation. The density of MgO paste at 1.1 and 0.9 w/b was measured to be 1600 and 1630 kg/ m<sup>3</sup>, respectively. Thus, the minimum static yield stress required for the bottom layer to sustain the load of consecutive layers was estimated to be 373 Pa using the relationship  $\sigma_v \ge \sigma_0 = \rho g h$  where  $\sigma_v$  is the static yield stress,  $\sigma_0$  is the stress at the first layer,  $\rho$  is density, g is the constant gravity acceleration (taken as  $9.8 \text{ m/s}^2$ ) and h is the height. Given the NC contents examined in this study and that the previous equation is a conservative estimate as it excludes additional structural buildup due to hydration or surface tension of thin layers [64], mixes with static yield stresses of 360 and 365 Pa were chosen to meet the printing requirements to produce 25.4  $\times$  25.4 mm cylinders. The MC content was chosen based on the lowest content in this study that produced high print quality, as discussed later in section 3.2. The NC and MC dosages to achieve the static yield stress and print quality for 1.1 and 0.9 w/b were found to be 3 wt% NC + 1.5 wt% MC and 1.75 wt% NC + 1.0 wt% MC, respectively. Cast specimens were prepared with and without the same corresponding dosage of additives at both w/b ratios in 25.4  $\times$  25.4 mm cylindrical molds and demolded after 24 h. 3D printed specimens were printed using a syringe gantry system with layer height and width of 1.55 mm. A minimum of four specimens were prepared for each test and all specimens, cast and 3D printed, were covered in plastic wrap for the first 24 h to mitigate water evaporation while being kept in the ambient lab environment. After 24 h, specimens to be carbon-cured were placed in a  $CO_2$  incubator at 20 %  $CO_2$ , 25°C and 80  $\pm$  5 % relative humidity (RH). Control specimens were also cured at 25°C and 80  $\pm$  5 % RH, but with  $CO_2$  at ambient levels ( $\approx 0.041$  %).

# 2.3. 3D printing

Cylindrical specimens with 25.4 mm outer diameter were printed

**Table 1**Chemical composition and physical properties of the supplied MagChem-30.

| Chemical composition (%)                       |     |                                     |                                |                                |      |                      | Loss on               |  |  |
|--|-----|-------------------------------------|--------------------------------|--------------------------------|------|----------------------|-----------------------|--|--|
| MgO  | CaO | $SiO_2$                             | Fe <sub>2</sub> O <sub>3</sub> | $Al_2O_3$                      | Cl   | SO <sub>3</sub>      | ignition (LOI)        |  |  |
| 98.2   | 0.8 | 0.35                                | 0.15                           | 0.10                           | 0.35 | 0.05                 | 1.7%                  |  |  |
| Physical properties                            |     |                                     |                                |                                |      |                      |                       |  |  |
| Loose bulk<br>density (g/<br>cm <sup>3</sup> ) |     | Median<br>particle size<br>(micron) |                                | Surface<br>(m <sup>2</sup> /g) | area | Activity index (sec) | % Passing<br>325 mesh |  |  |
| 0.35   |     | 3–8                                 |                                | 20-30                          |      | 18                   | 99                    |  |  |

using a syringe gantry printer built in-house with a nozzle diameter of 1.55 mm and movement speed of 40 mm/sec. The printed configurations are summarized in Table 2 and the printer used is shown in Fig. 1. Infills #1 and #2 are open infills with infill density less than 100 % providing continuous hollow paths along the height whereas infill #3 is a closed infill at 100 % infill density made of concentric circles and is intended to mimic cast specimens. These two infills were selected to study whether any strength differences between open and closed infills are due to increased carbonation of the interior elements. Infill #2 was introduced in addition to infill #1 to examine the effects of load transfer on strength for printed specimens with infill density less than 100 %. Additionally, shells (without any infill) were printed and tested: shells of infills #1 and #2 have an average thickness of 2.85 mm whereas infill #3 shell has an average thickness of 3.1 mm. The difference in thickness is caused by different line overlap parameters to achieve the required geometries.

Up to twelve specimens were prepared for each geometry and the mechanical results reported are the average of four specimens at a minimum. For sample sizes greater than four, sampling was held at one standard deviation from the population mean where samples above or below the standard deviation of the population were discarded as long as the sample size was maintained at four. The printing path was generated to achieve continuous printing of the complete specimen without any lifting or line crossing. This inadvertently resulted in skewing of the circular geometry to a more elliptical one, but with a variation of diameter of only 3–7%. When calculating strength, the average of both diameters was used for area calculations. Additionally, the area was assumed to be that of a full cylinder rather than the effective area for infills #1 and #2 to represent the cylindrical element strength rather than the specific material's properties.

### 2.4. Rheological characterization

A HAAKE MARS III rheometer with a 21.9 mm 4-blade vane and a 26.6 mm inner diameter cup was used to study the effects of NC and MC on the rheology of MgO paste. NCs were magnetically stirred into solutions at their respective content at 400 rpm for a minimum of 5 min while MC was dry-mixed with the MgO powder manually. The NC solution was used immediately after stirring and added to the premixed MgO + MC powders. Pastes were mixed for exactly two minutes using a handheld mixer and the testing setup was controlled to start the rheological protocol 11 min from time of adding solution to dry powder to ensure similar shear history. All tests were performed at 25°C with the test protocol shown in Fig. 2. All tests reached steady state by 1200 s and the plastic viscosity was recorded during steady state. New fresh pastes



Fig. 1. Syringe 3D printer system used in this study to produce all printed elements.

were prepared for each test to ensure similar shear history. The static yield stress was measured to be the peak stress response from applying a low, constant strain rate while the macroscopic elastic modulus was measured to be the slope of the stress–strain response within the linear region prior to yield within a strain range of  $10^{-2} - 10^{-1}$ .

### 2.5. Mechanical, chemical and optical characterization

For compressive strength testing, all specimens were capped using gypsum slurry to minimize confinement effects of the steel loading plates of the testing machine and to achieve smooth and parallel top and bottom surfaces for uniform axial loading. Tests were performed using an MTS Criterion C43 Electromechanical Testing Machine at a loading rate of 1.27 mm/min.

Mechanical testing results were supplemented by chemical characterization to confirm carbonation and identify the carbonation products. For this purpose, roughly cubic samples of 2 mm were obtained from the outer surface and from around the central axis, both at halfway height, of the tested specimens. In cases where the tested cylinder's failure mode prevented accurate sampling around the central axes, discs extracted by sawing unbroken cylinders were used where the outer surface was sanded off. Prior to sanding, these extracted discs were also used for optical microscopy using a Keyence VHX-5000 Digital Microscope. The products of outer surface sampling are referred to as exterior samples whereas those collected around the central axis are referred to as center samples for simplicity. All samples for characterization were pulverized using a mortar and pestle, and powder passing through a 53 µm sieve was collected. Qualitative chemical characterization was conducted via X-ray diffraction (XRD) and thermogravimetric analysis (TGA). The XRD was conducted using Malvern Panalytical XPert<sup>3</sup> powder diffractometer. Powdered samples were packed into a circular sample holder and exposed to  $\text{Cu-K}\alpha$  radiation with generator conditions at 40 V and 40 mA. The range of  $2\theta$  angles considered for the current study was  $5^{\circ}$  to 80°. Scans were run at a step size of 0.04° and step interval of 0.05 s per step. For TGA, 15 mg of the sample powder was placed in Thermal Instruments' TGA Q50 thermogravimetric analyzer to observe mass loss when the sample was heated from room temperature to 1000°C in an inert N<sub>2</sub> atmosphere at a rate of 20°C/min.

### 3. Results

### 3.1. Rheological measurements

The results of static yield stress of MgO paste at 1.1 and 0.9 w/b with different MC and NC contents are presented in Fig. 3. MgO paste at 1.1 and 0.9 w/b ratios have low static yield stresses of 2.4 and 10.4 Pa, respectively. In fact, at such low values the MgO paste can be considered to be a non-yield stress suspension, practically speaking. Addition of NC increases the static yield stress of MgO paste at 1.1 and 0.9 w/b at rates of 120 and 184 Pa per 1 wt% NC, respectively, as shown in Fig. 3; thus, transforming a non-yield stress paste into a relatively high yield stress paste that is suitable for 3D printing. Addition of MC alone increases the static yield stress at much lower efficiency - 1.3 and 9 Pa per 1 wt% MC for 1.1 and 0.9 w/b ratios, respectively. Overall, addition of MC to MgO paste with NC shows higher increase in static yield stress than NC alone up to 3 and 2 wt% MC at 1.1 and 0.9 w/b ratios, respectively. Doubling the content of MC either inhibits further increase or decreases it to similar levels as NC alone. Such effects were observed to greater extents in Portland cement systems, where MC increased NC efficiency in increasing the static yield stress up to a critical dosage threshold [60].

The elastic modulus was measured as the slope of the stress–strain diagram within strains in the range of  $10^{-2}$  –  $10^{-1}$  and the results of the effect of NC and MC on MgO paste are shown in Fig. 4. The increase in static yield stress due to the addition of NC correlates to an increase in the elastic modulus proportional to NC content, as shown in Fig. 4. The increases in elastic modulus at 1.1 and 0.9 w/b are 9.5 and 4.4 kPa per 1

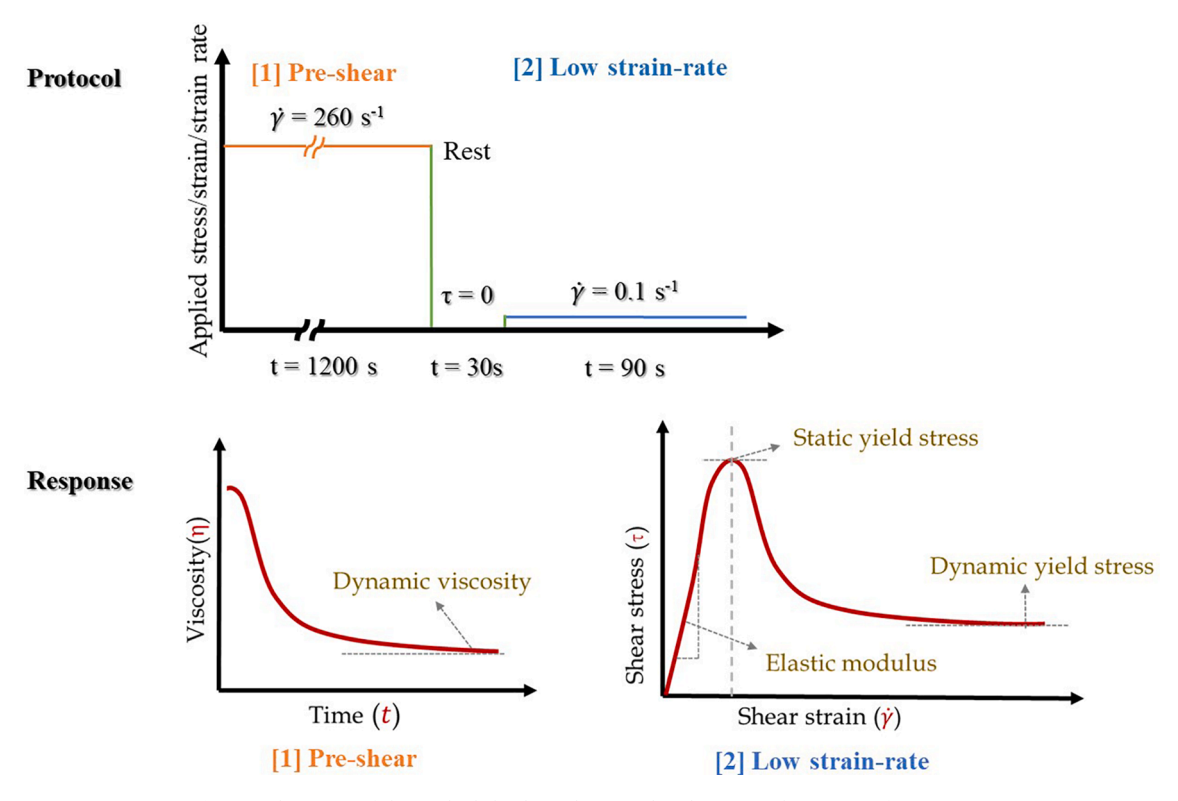


Fig. 2. Schematics of the applied rheological protocol and associated response of MgO paste.

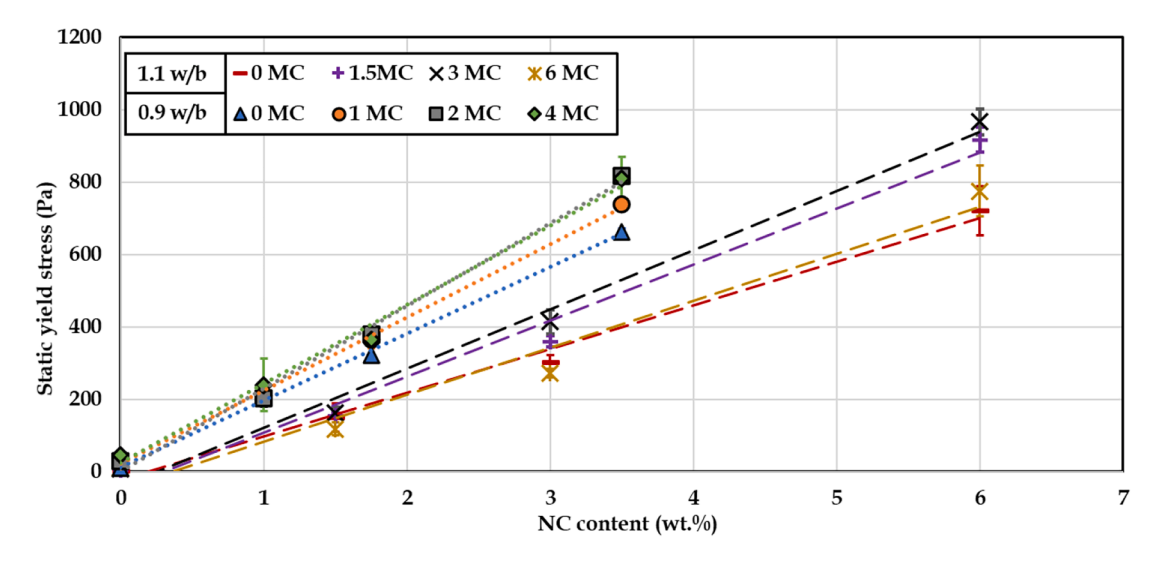


Fig. 3. Static yield stress measurements of MgO paste at 0.9 and 1.1 w/b ratios.

wt% NC, respectively. Addition of MC with NC, irrespective of MC content, led to lower increase in elastic modulus per 1 wt% NC content by 47 % and 57 % for 1.1 and 0.9 w/b, respectively. Because the change in MC content does not manifest in a significant change in the elastic modulus of either neat or NC-modified MgO paste, it could imply that MC causes a relaxation of the colloidal network due to stretching and uncoiling of the polymer coils [65,66], steric hinderance due to adsorption [67] or the collapse of the van der Waals network [68]. The critical concentration at which any of these phenomena occurs is outside the scope of this work and remains a subject of future investigation, but it is suspected to be lower than the lowest examined content at each w/b ratio.

The results of plastic viscosity are shown in Fig. 5 where neat MgO

pastes at 1.1 and 0.9 w/b ratios were recorded as having viscosities of 0.83 and 0.26 Pa.s, respectively. Addition of NC alone increases the plastic viscosity of MgO paste by 0.2 Pa.s per 1 wt% NC irrespective of w/b ratio whereas addition of MC alone increases it by 0.27 and 0.38 Pa. s per 1 wt% MC for 1.1 and 0.9 w/b, respectively. Addition of MC in NC increases the effect of NC on viscosity to 0.25 Pa.s per 1 wt% NC. While an increase in viscosity is generally unfavorable for 3D printing, the addition of cellulose ethers such as MC enhances consistency [69,70] and cohesion [71,72]. Pastes at the highest viscosity of 3.5 Pa.s were still extrudable using the printer system used in this study. Furthermore, the effect of NC and MC on viscosity are marginal compared to the increase in static yield stress where the rate of increase per 1 wt% NC in static yield stress is 38 and 62 times that of viscosity at 1.1 and 0.9 w/b ratios,

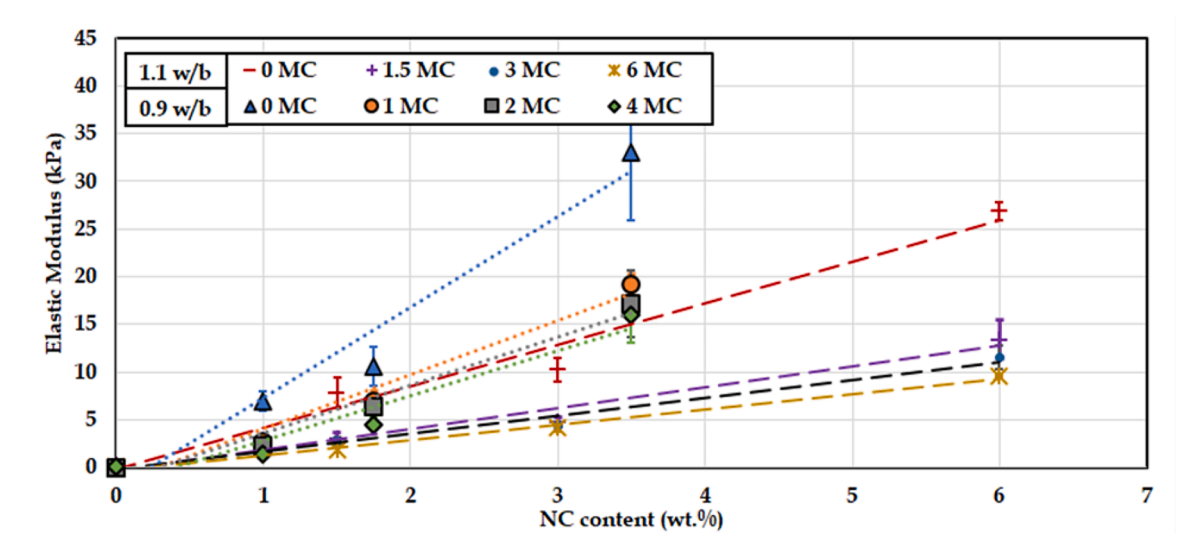


Fig. 4. Elastic modulus measurements of MgO paste at 1.1 and 0.9 w/b ratios.

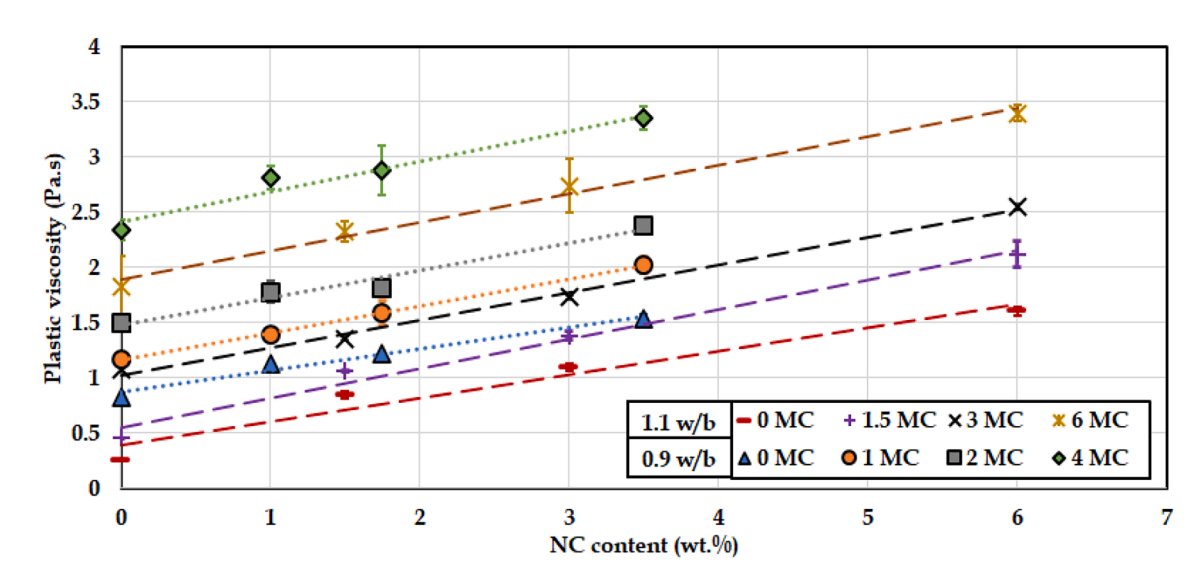


Fig. 5. Plastic viscosity measurements of MgO paste at 1.1 and 0.9 w/b ratios.

respectively.

## 3.2. Printing performance

To test the individual/combined effects of NC and MC on print quality, a rotating spirograph structure shown in Fig. 6 (a) was printed using different doses of only NC (Fig. 6 (b)), only MC (Fig. 6 (c)) or the combination of both (Fig. 6 (d)). The doses of NC or MC in Fig. 6 (b) and (c) were selected to magnify the effects of each additive on print quality for illustrative purposes. Those defects, highlighted by the red arrows, are still observed at the lower content but are so at a lower frequency or lesser extent. Fig. 6 (b) shows, as discussed previously in section 1, that defects associated with NC are caused by stiff filaments resulting in tearing and splitting. On the other hand, defects associated with MC are about poor buildability and shape stability (Fig. 6 (c)). The dosage in Fig. 6 (d) is the combination of the lowest NC and MC contents at 1.1 w/ b ratio which produce a high-quality print free of defects. While the addition of MC into NC-modified MgO paste did not show significant increase in static yield stress, as shown in Fig. 3, the effect of MC on print quality, likely linked to the decrease in elastic modulus and increase in viscosity (shown in Fig. 4 and Fig. 5, respectively), highlights the key role of utilizing VMAs in producing printable filaments. The combination of NC and MC produced filaments with higher cohesion without sacrificing extrudability, buildability or shape stability. Thus, to produce 3D printed elements for testing, NC and MC dosages were selected from the investigated ranges to meet the buildability stress requirement of 373 Pa alongside the lowest MC content to produce high print quality. The corresponding mixes selected were 3 wt% NC + 1.5 wt% MC at 1.1 w/b, which exhibited a static yield stress of 360 Pa, viscosity of 1.38 Pa.s and elastic modulus of 4.78 kPa, and 1.75 wt% NC + 1 wt% MC at 0.9 w/b, which maintained a similar static yield stress of 365 Pa, viscosity of 1.59 Pa.s and elastic modulus of 6.96 kPa.

Table 3 shows all the tested specimens with reference to the configurations presented earlier in Table 2 in addition to photos before and after carbon curing for 28 days. As mentioned previously, printed specimens had a slightly distorted circular geometry. This was significantly exacerbated by the inseam lines for infill #3 where it was alternated at  $180^{\circ}$  on the same neutral axis causing a stretch in that direction. The inseam for both infills #1 and #2 was rotated by  $3^{\circ}$  for every subsequent layer. The accumulation of the inseam for 16 layers (total of  $48^{\circ}$ 

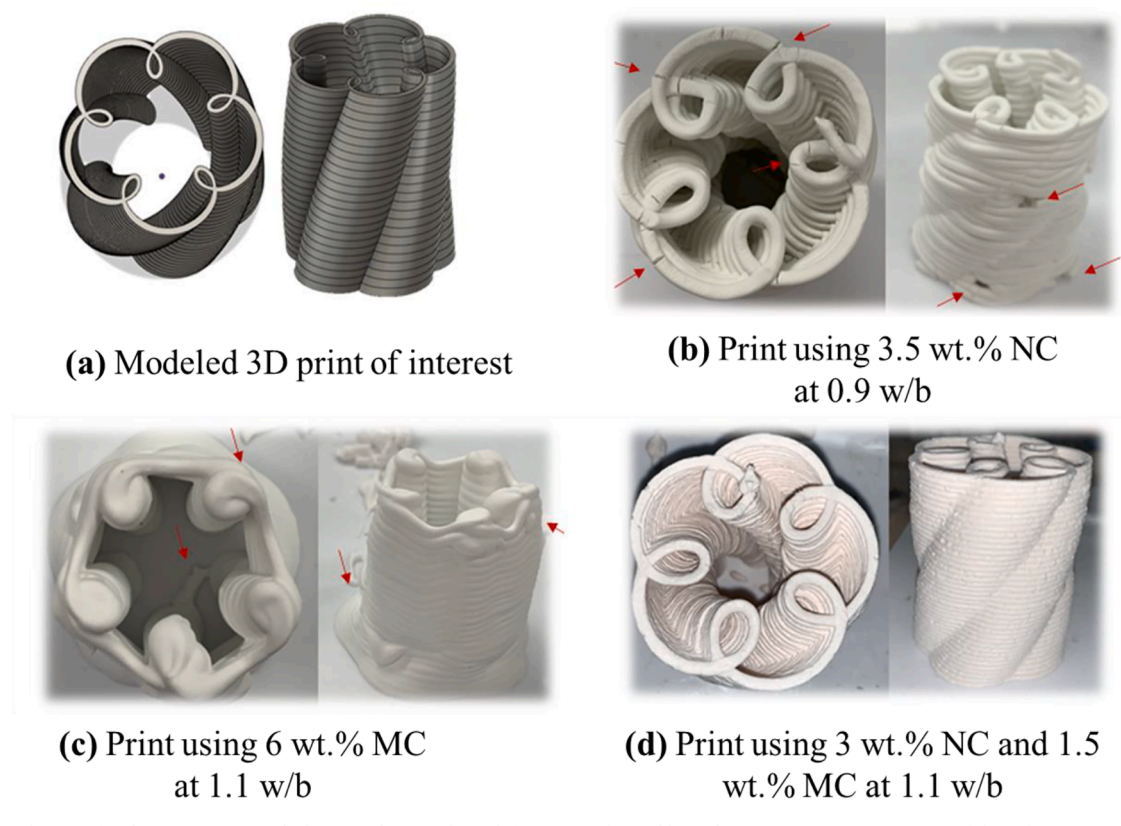


Fig. 6. Print quality test for (b) NC, (c) MC, and (d) NC with MC, where defects are indicated by red arrows. (For interpretation of the references to color in this figure legend, the reader is referred to the web version of this article.)

**Table 2**3D model illustrations of the print infill type showing dimensions, printing paths, and detailed views.

|               | Infill #1 (open) | Infill #2 (open) | Infill #3 (closed) |
|---------------|------------------|------------------|--------------------|
| Cross-section | 3° 25.4mm        | 30               |                    |
| 3D view       | 25.4mm           |                  |                    |

rotation of the top layer compared to the first layer) caused a stretch in the direction of the inseam. Some residual deposition from the inseam at the last layer protruded from all specimens, which was removed prior to testing and the surfaces were flattened and capped. After carbon-curing, a distinct change in color of the specimens from white (the color of the precursor MgO powder) to light yellow or off-white is observed, which could indicate carbonate formation as this change is not observed in the specimens cured in the low-CO<sub>2</sub> environment. Some white spots were observed on the carbonated 3D printed elements which were later identified as unhydrated MgO and are further discussed in the analysis of XRD results.

### 3.3. Compressive strength results

# 3.3.1. Cast specimens - role of admixtures and carbon curing

The goal of this study was to examine whether enabling 3D printing of MgO cement can increase  $\mathrm{CO}_2$  intake and subsequently increase compressive strength. The dosages of NC and MC in both 1.1 and 0.9 w/b ratios were selected to maintain a similar static yield stress while maintaining high print quality. As a result, the dosages of NC and MC are different between the two w/b ratios, which may impact compressive strength differently. To characterize such effects, cast specimens were prepared with and without admixtures at their respective w/b ratios and

**Table 3**Top view of different sample configurations; carbonated specimens are cured for 28 days. All residual inseams were removed and flattened prior to capping to ensure uniform loading conditions.

|                     | Infill #1 (open) | Infill #2 (open) | Infill #3 (closed) | Cast |
|---------------------|------------------|------------------|--------------------|------|
| Cross-<br>section   |                  |                  |                    |      |
| Ambient curing      |                  |                  |                    |      |
| After carbon curing |                  | 24.4             |                    |      |

tested for 3- and 28-day strengths and the results are shown in Fig. 7. For a given w/b ratio and curing condition, the change in compressive strength due to admixtures is insignificant except in two cases. The first is at 3 days: when admixtures are included at 0.9 w/b ratio, the carbon-cured specimen shows a decrease in strength of 38 %. The second is at 28 days where addition of admixtures at 1.1 w/b ratio shows an increase of 61 % of carbon-cured specimen. The increase in strength in 1.1 w/b specimens is likely caused by the improved shape retention with admixtures preventing early deformation of the low static yield "Neat" specimen after demolding, as shown in Fig. 7. On the other hand, it is unclear what caused the decrease in strength at 0.9 w/b with the addition of admixtures. Because the strength of Neat specimens and of ones with admixtures at 28 days are similar, the addition of admixtures

could have retarded early strength development up to 3 days. In fact, the Neat at 0.9 w/b reaches 93 % of the 28 days strength by 3 days. Thus, to rule out the effects of admixtures, all printed specimens will be compared to cast counterparts at the same corresponding dosage of admixtures.

For a given curing condition, whether admixtures are used or not, reducing the w/b ratio of MgO pastes shows higher compressive strength at younger age [73], similar to Portland cement. More notably, all carbon-cured specimens show an increase in compressive strength over their air-cured counterparts, as expected. The increases are 710 % at 3 days and 1280 % at 28 days for 1.1 w/b ratio, and 310 % at 3 days and 390 % at 28 days for 0.9 w/b ratio. This confirms that accelerated carbonation is crucial for compressive strength development of MgO

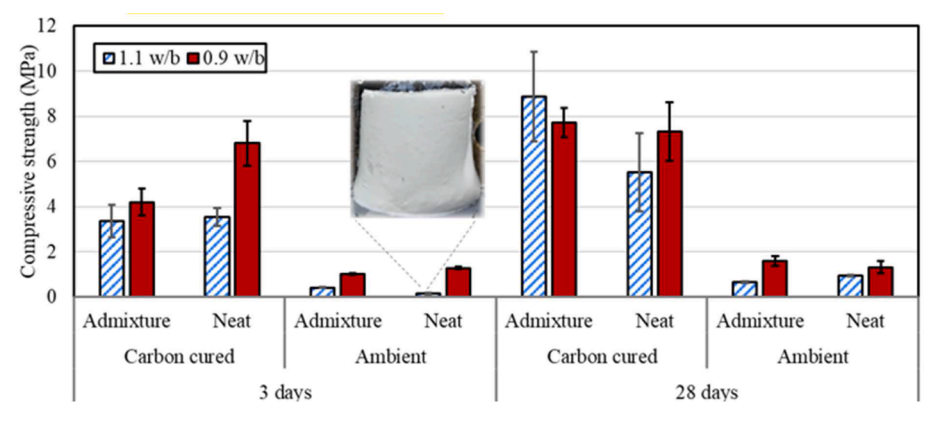


Fig. 7. Compressive strength of cast specimens with ("Admixture") and without ("Neat") admixture.

concrete and that the need to increase carbon intake and its rate is vital. Therefore, the rest of the discussion will be focused on the effects of 3D printing on compressive strength of only carbon-cured specimens.

### 3.3.2. 3D printing effects

The results of compressive strength of 3D printed versus cast specimens are shown in Fig. 8 and indicate higher compressive strength of printed specimens over their cast counterparts. The maximum increases are 525 % at 3 days and 432 % at 28 days for 1.1 w/b ratio with infill #2, and 455 % at 3 days and 390 % at 28 days for 0.9 w/b ratio with infill #3, respectively. Because MgO paste gains mechanical strength through carbonation, the increase in strength of 3D printed specimens over their cast counterparts can be directly attributed to higher carbon intake leading to higher content of magnesium carbonates. Differences in strength between the infill patterns can be attributed to either differences in carbon intake or load bearing capacity. While the degree of carbonation is further investigated by the recorded mass change and chemical characterization in sections 3.4, 4.2 and 4.3, the bearing capacity and, more specifically, stress transfer can be examined by comparing the infill patterns at 1.1 w/b ratio. Infill #2 may be recalled consisting of six channels compared to the four of infill #1. Since both open infills expose the interior structure to atmospheric conditions including carbon curing, the changes in mechanical strength between infills #1 and #2 are influenced by differences in load bearing capacity, stress transfer mechanism, and/or carbon intake. However, 3D modeling of both infills reflect only 5 % change in the exposed surface area due to filament thickness and line overlapping parameters. Thus, the differences in strength between both infills are more likely due to changes in stress transfer or load bearing capacity. Since both infills #1 and #2 were not designed using topological optimization, it is safe to assume that optimum stress transfer is achieved with a solid 100 % infill such as in infill #3. Because the strength of cylinders with infill #2 and infill #3are statistically indifferent, maintaining similar strength with lower infill density such as infill #2 indicates maintaining optimum stress transfer. Further decrease in infill percentage at infill #1 however results in a decrease in strength, suggesting the likelihood of stress concentrations, worsened stress transfer or reducing bearing capacity. Stress analysis using finite element mapping local carbonates locations is needed to further investigate those differences and is subject to future research.

Comparing the effects of w/b ratios of similar infills, 0.9 w/b specimens show higher compressive strength at 3 days whereas statistically there is no difference in the strengths at 28 days between the two w/b ratios. This corresponds to a significantly higher rate of strength

development from 3 to 28 days for specimens at 1.1 w/b (by 103 % and 175 % for infills #1 and #3, respectively) compared to 0.9 w/b (by 47 % and 62 % for infills #1 and #3, respectively). The authors suspect this to be due to differences in porosity between the two [74]. Since all specimens are cured at 80 % RH, water evaporation due to drying continues to occur for the duration of curing. The specific gravities of MgO and brucite are 3.58 and 2.37 [7], respectively, while those of some of the magnesium carbonates are less than 2.25 [75]. Thus, the conversion of MgO to brucite and subsequently to magnesium carbonates involves a sequential increase in solid volume. The resulting expansion leads to a denser microstructure filling up capillary pores and reducing  $CO_2$ penetration, as a function of the reduced permeability. Because specimens made with 1.1 w/b have higher water content, a higher capillary porosity is expected at early ages of curing where water evaporation is expected to occur at a higher rate than carbonation. As curing continues, the higher porosity aids CO<sub>2</sub> penetration and creates more space for magnesium carbonates to form.

### 3.3.3. Strengths of shells and cores

Carbonation is a function of permeation, diffusion and crystal growth potential, all of which are positively impacted by greater porosity. Therefore, to further investigate the role of w/b ratios on porosity, and subsequently on carbon intake and compressive strength, additional cylindrical specimens representing the shells and cores of infill #3, a solid/closed infill, were tested for compressive strength after 28 days of carbon curing. The representative shell ("Infill #3 - shell") involved printing two concentric circles, creating a hollow cylinder with 25.4 mm outer and 19.7 mm inner diameters and a height of 25.4 mm. "Reduced" cores are essentially carved-out cores, prepared by first printing 25 mm infill #3 specimens, carbon-curing them for 28 days as before, and finally sanding them down uniformly to remove the outer 'shell' volume (2.7 mm from all surfaces) to create smaller cylinders of 20 mm diameter and height. These provide a clue to physical and mechanical properties of the interior of the specimens where the carbon penetration is hampered by the exterior. To get an understanding of how the interior would have performed with an ideal, 100 % porous exterior, representative or "Simulated" cores, also with 20 mm diameter and height to compare with the reduced cores, were intended to be produced. However, because the regular 25.4 mm specimens were too soft to be sanded prior to carbon curing (after 24 h of printing), the simulated cores were prepared instead by printing 20 mm diameter and height cylinders with the same line parameters as for reduced cores and were carbon cured for 28 days before testing.

The results of all specimens are shown in Fig. 9 supporting previous

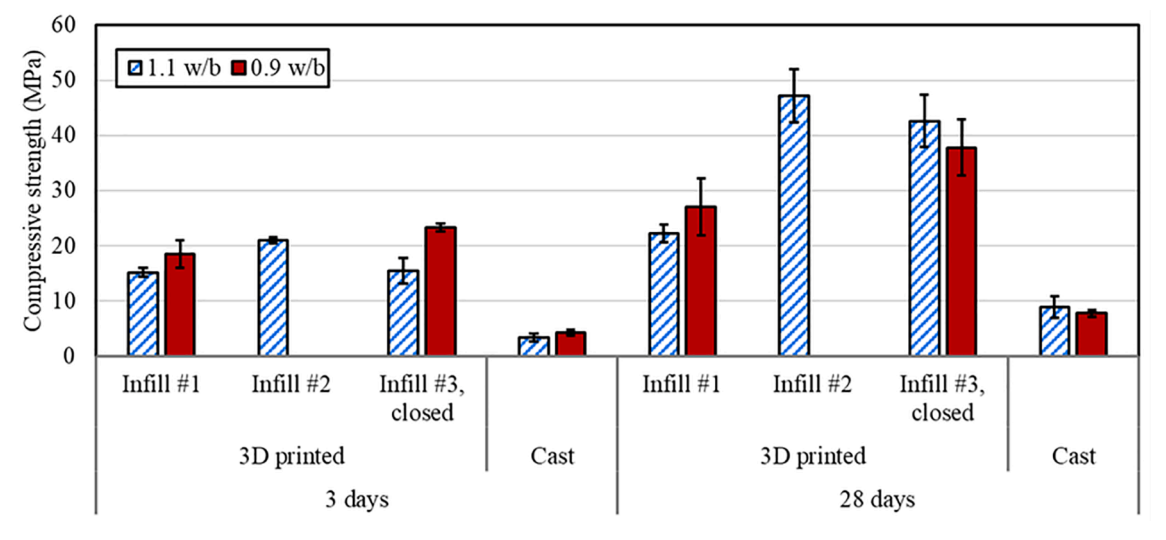


Fig. 8. Compressive strength results of 3D printed specimens compared to cast specimens.

observations that higher w/b ratio correlates with higher compressive strength after 28 days of carbon curing for the printed, unprocessed specimens. Since strength gain is a direct result of carbonation, a higher strength at higher w/b ratio suggests a positive correlation between increasing w/b ratio and carbonation. This relationship is maintained in the simulated cores. While shells prepared at 0.9 w/b ratio show similar strength to the closed infill specimens, shells at 1.1 w/b show an increase in strength. Shell specimens have better exposure to CO<sub>2</sub> due to the higher surface area to volume ratio as compared to core specimens and can thus undergo more carbonation. For closed specimens, once the exterior is fully carbonated, little to no further carbon penetration or diffusion to the core is expected. The processed specimens, i.e. the reduced cores, show the opposite trend where the higher w/b ratio specimens had lower strengths than the lower w/b ones. This effect can be directly attributed to carbonation rather than size-effects as simulated cores maintain similar behavior to those of infill #3 at the larger size. On the other hand, higher compressive strength is observed at 1.1 w/b compared to 0.9 w/b for simulated cores contrary to reduced ones. The increased water evaporation at higher w/b prior to carbonation results in higher porosity that increases carbonation at the shells. After the shells carbonate, little carbon diffusion occur at the core leaving more porous cores at 1.1 w/b compared to 0.9 w/b which could explain the change in strength trend observed.

### 3.4. Mass change

The mass of carbon-cured and ambient condition specimens was recorded at 1, 3 and 28 days. The relative humidity in both conditions is less than 100 %, which should cause evaporation of water and lead to a decrease in specimen mass. On the other hand, carbonation will increase the specimen mass due to absorption of carbon dioxide to form magnesium carbonates. The change in mass of carbonated specimens should then be the increase in mass due to carbonation combined with the reduction in mass due to water evaporation. Ideally, the loss of water for all specimens can be estimated by the change in mass just under ambient condition, since both conditions have the same temperature and RH. However, a confounding factor in the case of carbonated specimens is that the decreased surface porosity due to carbonation will impede water evaporation at later ages, deviating from the water loss of ambient condition specimens. Therefore, the analysis of change in mass shown in Fig. 10 is only qualitative to compare different infill patterns, effect of printing, and the change in w/b ratio.

The results show that all 3D printed specimens exhibit a higher mass increase due to carbonation than the cast specimens regardless of age, and no significant differences between infill patterns are observed. At 3 days age, there are no significant differences in mass change between

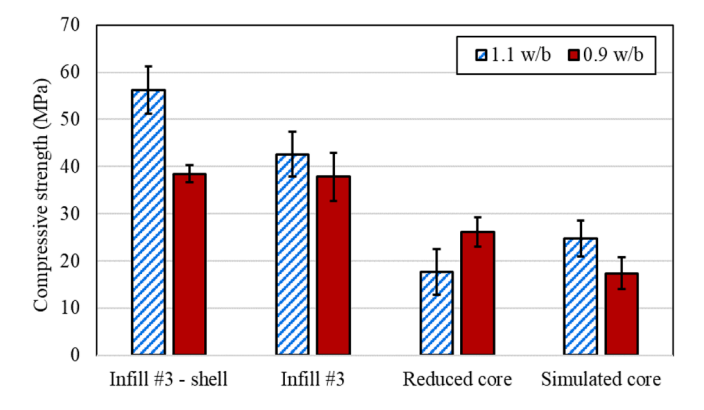


**Fig. 9.** Comparison of 28-day compressive strength of Infill #3 specimens with outer shell and inner cores (reduced and simulated). Infill #3 and the corresponding shell have an outer diameter of 25 mm, while the cores have an outer diameter of 20 mm.

both w/b ratios. However, at 28 days, all specimens (printed and cast) show higher mass increase at 1.1 w/b compared to 0.9 w/b ratio. These results support that higher w/b ratio leads to higher water loss increasing porosity and enhancing carbon penetration to yield higher compressive strength as discussed previously.

In order to study the effects of 3D printing on water evaporation only, a new set of specimens were prepared and stored at ambient conditions with the same relative humidity and temperature as for the carbon-cured ones. To exclude the effects of internal infill pattern this analysis is focused on only cast and infill #3 specimens. Because the exposed surface area conditions changed for cast specimen with demolding at 24 h, the results of mass change were recorded between 0 and 24 h separately from 1 to 3- and 28-days carbonation periods. The results are shown in Fig. 11 and clearly indicate that printed specimens lose more water on average than cast ones within the first 24 h. This is likely attributed to the higher exposed surface area of 3D printed specimen compared to that of cast which stay inside the casting molds. The greater mass loss of printed specimens by 64 % and 290 % at 1.1 and 0.9 w/b ratios leads to less available water for MgO hydration but also implies greater porosity.

Once the initial loss has occurred and both specimens are equally exposed to similar conditions, cast specimens show similar or greater mass loss at 3 and 28 days compared to 3D printed ones. This is likely attributed to the greater amount of free water available in cast specimen owing to lower water evaporation during the first 24 h. 3D printed specimens at 1.1 w/b undergo mass loss similar to or greater than that at 0.9 w/b, following similar analysis. On the other hand, while cast specimens at 1.1 w/b had greater initial loss than those at 0.9 w/b within the first 24 h, specimens at 1.1 w/b maintained greater water loss. This is likely caused by the reduced water loss due to the additional protection from the casting molds, which was immediately followed by carbonation and corresponding reduction in shell porosity due to the formation of carbonates, as discussed in section 3.3.2. Nevertheless, since the differences recorded at 1 and 3 days did not result in significant differences in strength compared to those observed at 28 days, and because water loss at 28 days is four times as that at earlier ages, it is likely that the level of water saturation of pores, which is expected to decline with age due to evaporation, has a significant impact on CO2 diffusion and, subsequently, on strength development.

# 4. Microstructural analysis

# 4.1. Visual differences and microscopy images

Fig. 12 shows a cast and a printed specimen after crushing. Some visual and textural differences are apparent after just 3 days of carbon curing. The exposed surfaces were hard to the touch and had a yellowish or off-white color characteristics. These were inferred to be associated with the crystallized magnesium carbonates as carbonation is expected at these locations. The interior had a flaky soft texture and white color and inferred to be either unhydrated MgO or brucite. These inferences are also based on the difference in color observed between carbonated and uncarbonated specimens in Table 3. To further investigate the visual differences, discs of 1.5-2 mm thickness were prepared of cast and 3D printed specimens that were carbon cured for 3 days at both 1.1 and 0.9 w/b ratios as shown in Fig. 13. The noted color difference identified visually between carbonated and uncarbonated areas can similarly be inferred as unhydrated MgO or brucite due to the white flaky and softtextured areas. Comparing both 1.1 and 0.9 w/b images, greater number of micropores and thicker dark shells can be identified in the 1.1 w/b specimens compared to 0.9 w/b specimens, which is in agreement with previous discussions on the positive correlation between greater water loss, higher porosity and improved carbon penetration. Nevertheless, the image analysis in this section remains speculative and conclusive classification of carbonated versus uncarbonated areas can be completed with the use of SEM EDS analysis and is subject to future work.

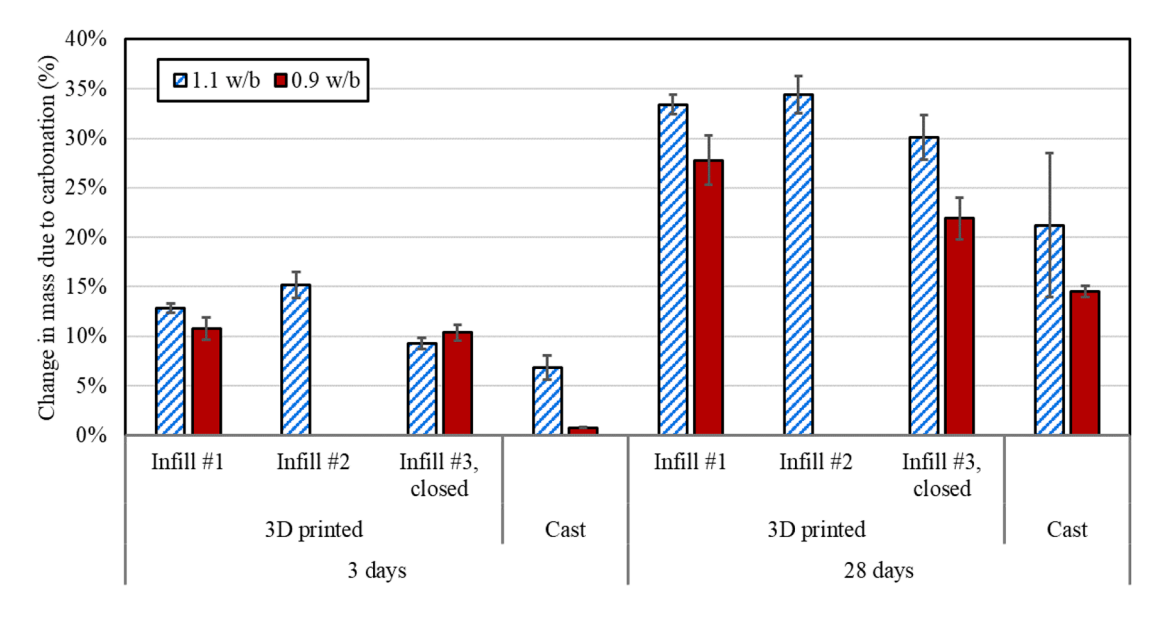


Fig. 10. Percentage change in mass due to carbonation where water evaporation losses were measured by recording mass change of similar specimens stored at ambient conditions.

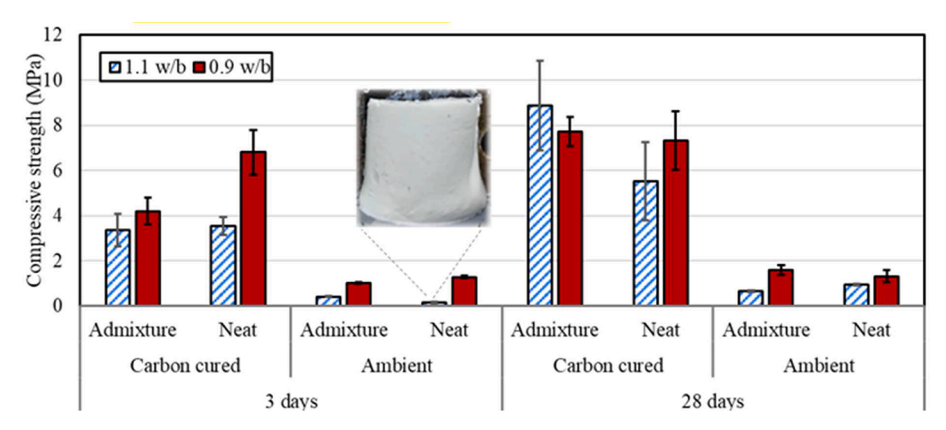


Fig. 11. Mass loss during initial molded time of cast specimen (0-1 day) and time period post demolding equal to carbon curing period (1-3 days; 1-28 days) where all specimens are stored at ambient condition.

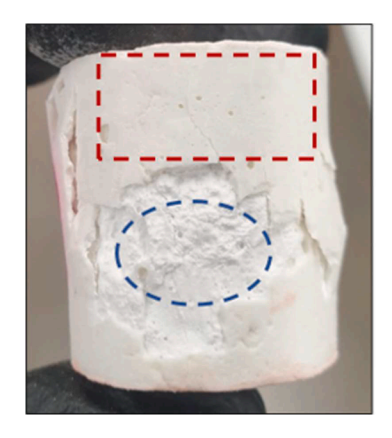
### 4.2. X-ray diffraction spectroscopy

Samples for X-ray diffraction were obtained as detailed earlier and several diffractograms are presented in Figs. 14, 15, 16 and 17. Because the depth of carbon penetration changes with w/b and curing age, exact separation of shells and cores of the tested specimens was not possible, deterring from quantitative XRD assessment. Thus, analysis in this section is focused on detecting and identifying the different magnesium carbonate phases, any unhydrated MgO or uncarbonated brucite. The samples for XRD analysis were collected from the tested cylinders whose strength was reported in the previous sections. Particle diffraction files were used to identify phases such as MgO (PDF#45-0946), brucite (PDF#44-1482), nesquehonite (PDF#20-0669), hydromagnesite (PDF#20-0669), dypingite (PDF#23-1218), magnesite (PDF#08-0479), calcite (PDF#5-586) and portlandite (PDF#44-1481) among others. Identification was based on the higher order peaks therein and these have been labeled where encountered.

Fig. 14 shows the XRD spectra of exteriors and centers of 1.1~w/b cast specimens that were carbon-cured for 3 and 28 days, in addition to the exterior of a 1.1~w/b cast specimen cured for 28 days at ambient conditions. No magnesium carbonates were detected in the exteriors of ambient condition specimen signifying that no carbonation occurs at either 3 or 28 days. Furthermore, since carbonation first occurs at the

exteriors, no magnesium carbonate products are expected in the center in this case. On the other hand, nesquehonite  $(2\theta=13.6^{\circ},\,23.1^{\circ})$  is detected in the exterior of the carbon-cured specimens as early as 3 days and also at 28 days, alongside some uncarbonated brucite  $(2\theta=38^{\circ},\,18.5^{\circ})$  at both ages. The centers at both 3 and 28 days showed very small peaks of nesquehonite and confirmed the earlier hypothesis that once the shell is carbonated, carbon penetration is greatly reduced. Because the cast specimen cured in the ambient  $CO_2$  environment showed no detectable magnesium carbonates even after 28 days, the rest of this analysis is focused only on carbon-cured specimens. Some calcite is also detected  $(2\theta=29^{\circ})$  possibly due to the CaO impurity in the MgO, but is irrelevant to the discussion in this study.

XRD spectra of the 3D printed infill #3 specimens at 1.1 w/b were examined at 3 and 28 days and are presented in Fig. 15. Similar to cast specimens, the exteriors show distinct evidence of magnesium carbonates in the form of nesquehonite as early as 3 days alongside uncarbonated brucite, whereas no magnesium carbonates are detected at the core. However, unlike in cast specimens, some unhydrated MgO ( $2\theta = 42.9^{\circ}$ ,  $62.3^{\circ}$ ) was also detected in both the exterior and the center of the printed specimens. As reported previously, 3D printed specimens show significantly higher water evaporation compared to cast ones in the first 24 h due to the difference in surface exposure/protection. The excessive water loss could prevent complete hydration of some of the MgO paste.



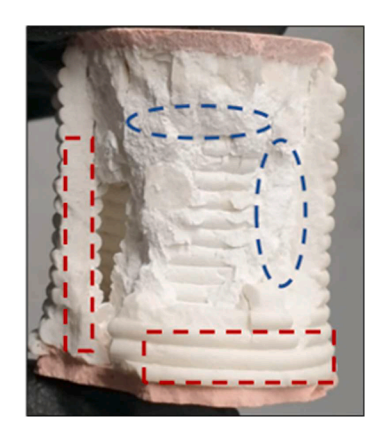


Fig. 12. Crushed cast (left) and infill#1 (right) cylinders at 0.9 w/b ratio exposing two visually different materials identified as magnesium carbonates with yellowish color (highlighted with red dotted line rectangles) and unhydrated MgO or brucite identified as white flaky powder (highlighted with blue dotted line ovals).

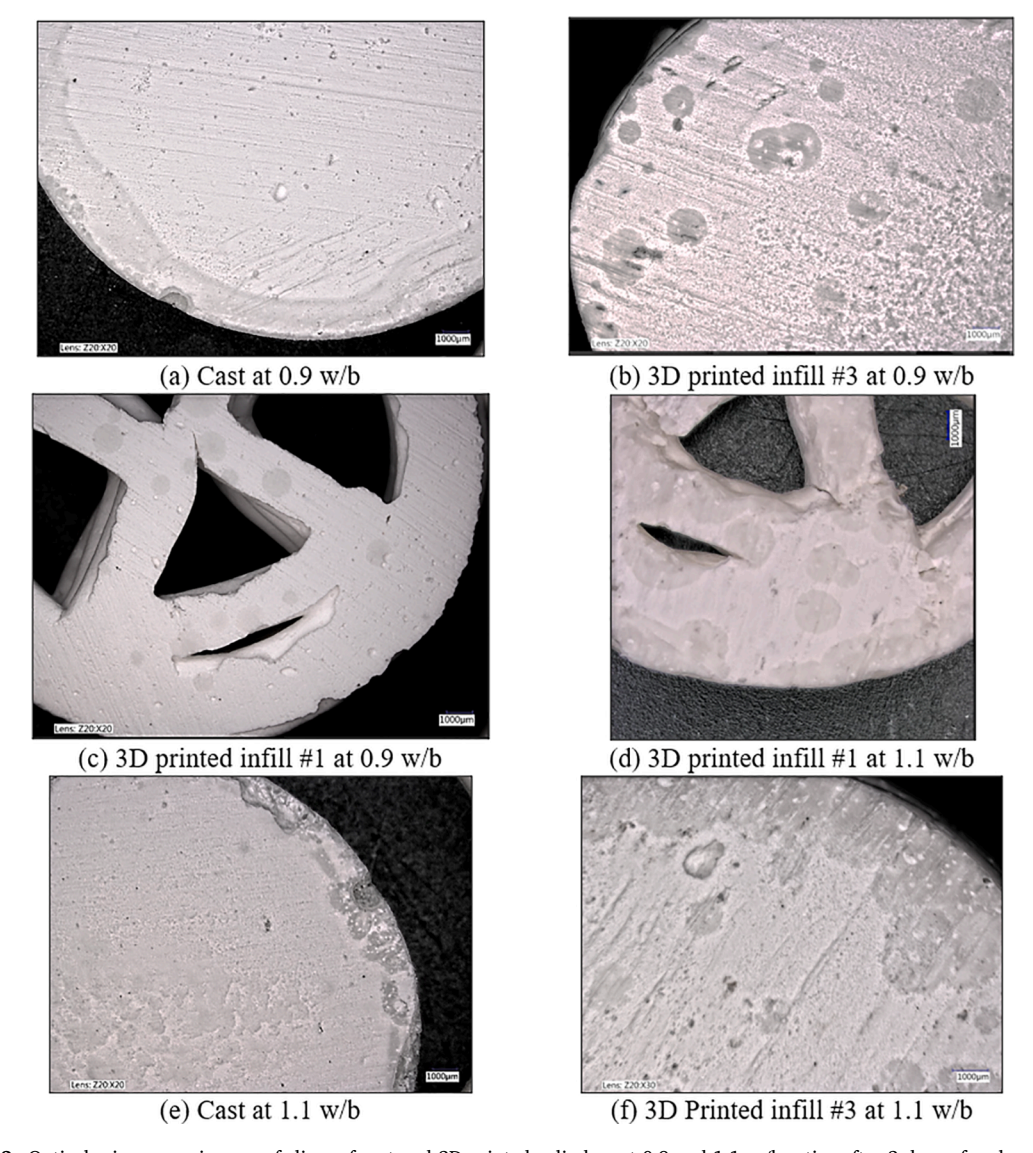


Fig. 13. Optical microscopy images of slices of cast and 3D printed cylinders at 0.9 and 1.1 w/b ratios after 3 days of carbon-curing.

Additionally, the conversion of MgO to brucite (Mg(OH)<sub>2</sub>) requires the molar ratio of H<sub>2</sub>O:MgO of 1:1 while the conversion of MgO to nesquehonite requires a higher molar ratio of H<sub>2</sub>O:MgO of 3:1. If carbonation is introduced while MgO is still within its primary hydration phase,

carbonation and hydration will compete for available water. Additionally, higher water evaporation could lead to higher porosity and subsequently higher degree of carbonation, further increasing the competition over pore water. Since specimens are first left at ambient

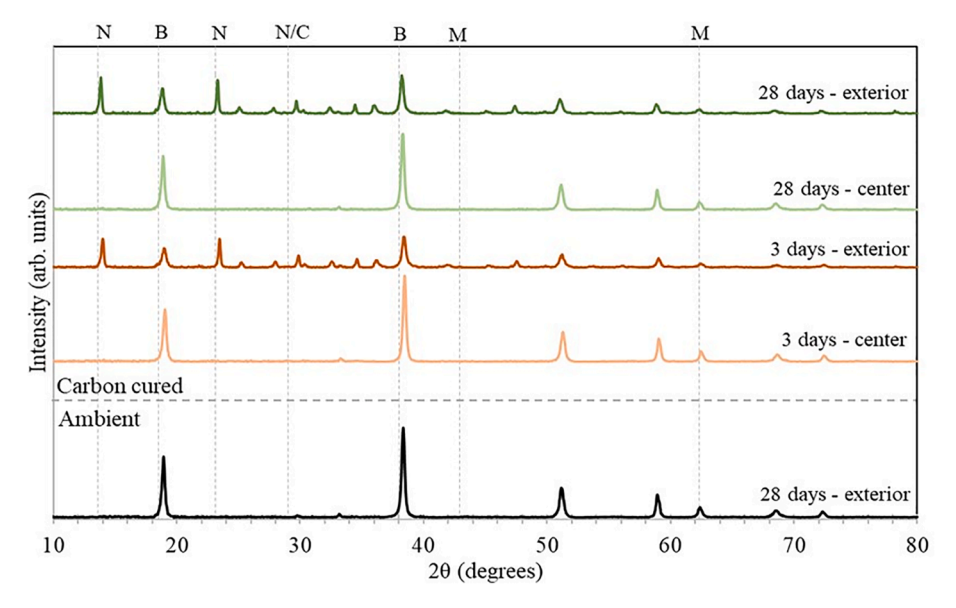


Fig. 14. Comparing the XRD spectra of surfaces of 1.1 w/b ratio cast specimens after 3 and 28 days of curing in air and CO<sub>2</sub> (B – Brucite, N – Nesquehonite, C – Calcite, M – MgO).

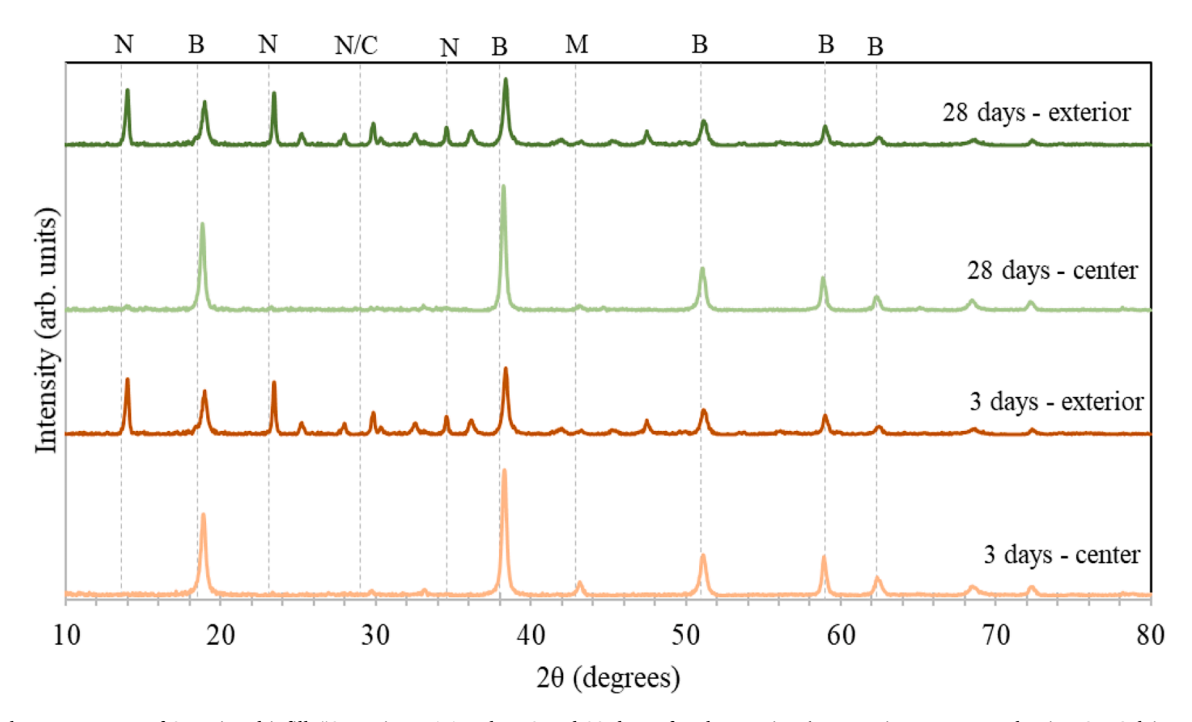


Fig. 15. The XRD spectra of 3D printed infill #3 specimen 1.1 w/b at 3 and 28 days of carbon curing (B – Brucite, N – Nesquehonite, C – Calcite, M – MgO).

conditions for the first 24 h before carbon-curing is introduced and because the MgO used in this study is light burned with high reactivity, it is more likely that the unhydrated MgO is primarily caused by the excessive evaporation while the increased water consumption from carbonation plays a secondary role. It is important to highlight that increasing the studied RH would likely yield similar results, as water loss was also reported by Vandeperre at 98% RH [76]. This however suggests that alternative cyclic curing methods that alternate replenishing water and carbonation could lead to higher levels of overall carbonation and mechanical performance [74].

Similar analysis for cast and infill #3 3D printed specimens was carried out for 0.9 w/b ratio specimens at 3 and 28 days and the results are show in Fig. 16 and Fig. 17, respectively. Additional scans of infill #1

3D printed specimen at 3 days of curing are also included in Fig. 17 to determine if any new carbonate peaks appear. The exteriors of cast and closed 3D printed specimens at 3 and 28 days show successful carbonation of brucite into nesquehonite with some uncarbonated brucite whereas the cores are composed of predominantly uncarbonated brucite. Unhydrated MgO were detected in both the exteriors and centers of 3D printed specimens similar to the results acquired for 1.1 w/b specimens. However, greater MgO relative peak intensity is observed at 0.9 w/b compared to 1.1 w/b specimens indicating the likelihood of greater quantity of unhydrated MgO. Such is expectedly caused by the reduced water content due to lower w/b ratio and greater water evaporation in the first 24 h as reported in Fig. 11. Additionally, some differences in water retention can be attributed to the different dosages of NC and MC

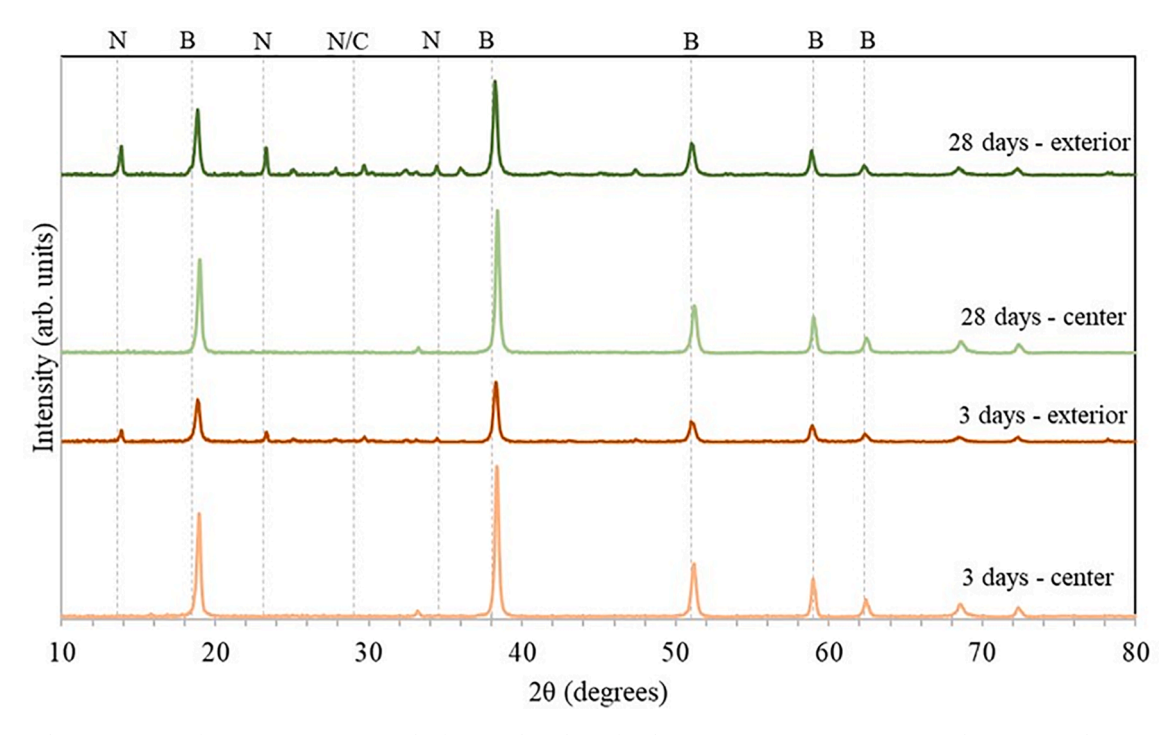


Fig. 16. The XRD spectra of cast specimen at 0.9 w/b after 3 and 28 days of carbon curing (B - Brucite, N - Nesquehonite, C - Calcite, M - MgO).

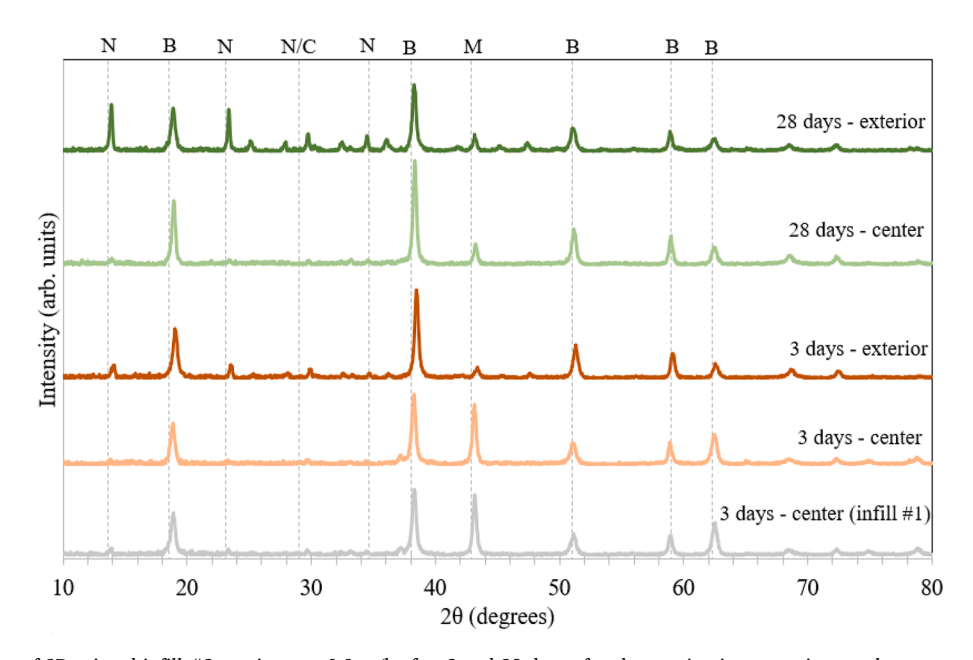


Fig. 17. The XRD spectra of 3D printed infill #3 specimen at 0.9 w/b after 3 and 28 days of carbon curing in comparison to the center of infill #1 after 3 days of curing (B – Brucite, N – Nesquehonite, C – Calcite, M – MgO).

used at each w/b ratio. However, the relationship between these two additives and water loss/retention remains outside the scope of this work but are topics of future research. Nevertheless, despite the presence of the significantly weak uncarbonated MgO, closed 3D printed specimens maintained much higher compressive strength than its cast counterparts indicating greater degree of carbonation. Higher surface exposure of the center in infill #1 did not reflect significant changes in peak intensities or reveal any new peaks, indicating that the observed increase in compressive strength of open infills #1 and #2 compared to cast ones is likely not due to increased surface exposure.

# 4.3. TGA

To further examine the degree of carbonation, TGA measurements of cast and infill #3 specimens after 28 days of carbonation were collected from the centers of tested specimens at 1.1 and 0.9 w/b ratios and the results are presented in Fig. 18. Hydrated magnesium carbonates begin to dehydrate at  $50^{\circ}$ C and continue until  $300^{\circ}$ C [77,78] at which infill #3 specimens lose 12 % and 14.7 % of their mass at 1.1 and 0.9 w//b ratios, respectively, whereas cast specimens lose 4.7 % and 2.3 %. This indicates the presence of greater amounts of hydrated magnesium carbonate in the printed specimens compared to their cast counterparts. This is further supported by the prevalent and larger peaks at  $530^{\circ}$ C for

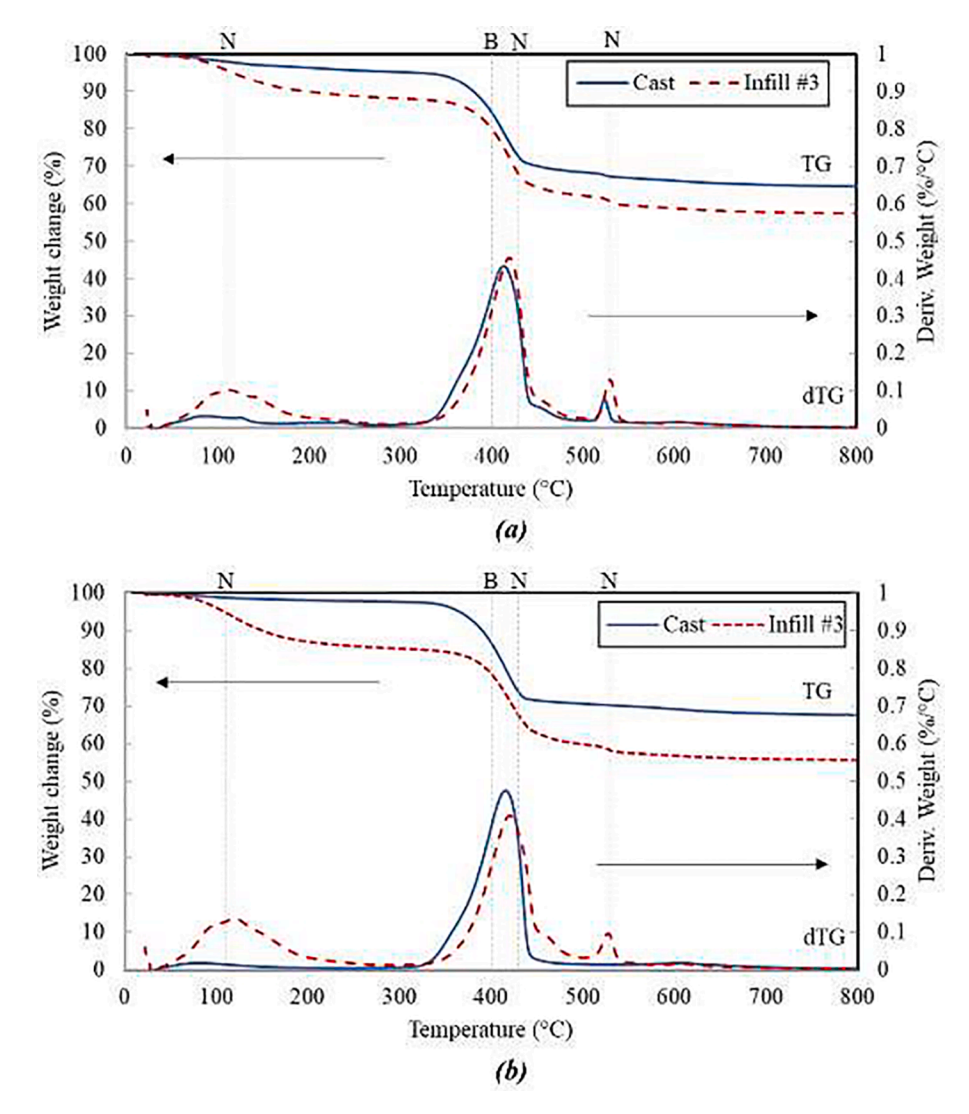


Fig. 18. TGA results of cast and infill #3 procured from the centers of tested specimens after 28 days of carbonation curing at (a) 1.1 w/b and (b) 0.9 w/b. Upper curves are weight change percentage and lower curves are derivative of weight change w.r.t. temperature (B: Brucite, N: Nesquehonite).

printed specimens compared to cast ones, which in addition to the previous peak correspond to the thermal decomposition of magnesium carbonates [79–81], more specifically nesquehonite, as previously indicated by XRD results and in agreement with findings of Ma et al [82]. In fact, infill #3 led to 7.3 % and 12.4 % greater mass loss by 550 °C compared to their cast counterparts at 1.1 and 0.9 w/b ratios, respectively. The TGA results indicate greater carbon intake, specifically at the interior, of printed specimens. Hence, it is likely that 3D printing effects such as interfilamentous and interlayer gaps could be improving carbon penetration, leading to thicker carbonated shells and higher load bearing capacity.

### 5. Conclusion

The aim of the study was to examine whether enabling 3D printing using admixtures such as NC and MC can improve carbonation of MgO paste leading to positive impact on compressive strength. The effects of adding MC and NC on the rheology of MgO paste at 1.1 and 0.9 w/b ratios were examined first. The dosage of NC and MC was then selected at each w/b ratio to maintain similar static yield stress and, as a result, similar buildability. Cast and 3D printed cylinders were prepared with open-to-air and closed (solid) infill patterns at each w/b ratio, which were carbon-cured for 3 or 28 days. The mass change of all specimens

was recorded for the first 24 h and for the curing duration. Finally, microstructural analysis was used to characterize magnesium carbonates at the shell and cores of tested specimens. The results support the following:

- The addition of NC as a rheological modifier is very effective in increasing the static yield stress of MgO paste. However, MC was needed as an additional additive to improve the cohesion and prevent filament tearing and splitting.
- Regardless of infill pattern, 3D printing is effective in increasing compressive strength of MgO paste, likely due to higher carbon intake, which can facilitate the production of elements with higher strength to weight ratio.
- To maximize the strength to weight ratio of printed MgO cylinders the infill patterns should be selected with greater emphasis on efficient stress transfer rather than carbon delivery potential.
- Higher water evaporation, often exacerbated by the lack of protective casing, leads to increased porosity, which can lead to subsequent increase in mechanical strength due to improved carbon delivery and greater available volume for the formation of magnesium carbonates.
- Increasing the w/b ratio of MgO paste yields higher 28 days compressive strength up to the studied 1.1 w/b ratio, likely due to

- the higher water loss potential and subsequent increase in porosity and carbon delivery.
- Carbon-cured 3D printed MgO paste cylinders reach a compressive strength of 40–60 MPa based on infill pattern and w/b ratio, which is sufficient for structural applications

### CRediT authorship contribution statement

AlaEddin Douba: Conceptualization, Methodology, Investigation, Formal analysis, Writing – original draft, Writing – review & editing, Visualization. Palash Badjatya: Methodology, Investigation, Formal analysis, Validation, Writing – original draft, Writing – review & editing. Shiho Kawashima: Methodology, Validation, Writing – review & editing, Supervision, Project administration, Funding acquisition.

## **Declaration of Competing Interest**

The authors declare that they have no known competing financial interests or personal relationships that could have appeared to influence the work reported in this paper.

### Acknowledgement

The authors would like to acknowledge the National Science Foundation (Award #1653419 and #2020095) and Columbia University's School of Engineering and Applied Science (SEAS) Interdisciplinary Research Seed (SIRS) Program for financial support, and the staff of Columbia University's Carleton Laboratory for technical support. The authors would also like to thank Active Minerals and Martin Marietta Magnesia Specialties for donating Acti-gel 208 and Magchem-30 for this investigation.

### References

- [1] M.E. Boot-Handford, J.C. Abanades, E.J. Anthony, M.J. Blunt, S. Brandani, N. Mac Dowell, J.R. Fernández, M.-C. Ferrari, R. Gross, J.P. Hallett, R.S. Haszeldine, P. Heptonstall, A. Lyngfelt, Z. Makuch, E. Mangano, R.T.J. Porter, M. Pourkashanian, G.T. Rochelle, N. Shah, J.G. Yao, P.S. Fennell, Carbon capture and storage update, Energy Environ. Sci. 7 (1) (2014) 130–189, https://doi.org/10.1039/C3E42350F.
- [2] C. Unluer, "Carbon dioxide sequestration in magnesium-based binders," in Carbon Dioxide Sequestration in Cementitious Construction Materials, Elsevier, 2018, pp. 129–173.
- [3] R.M. Andrew, Global CO2 emissions from cement production, Earth Syst. Sci. Data 10 (1) (2018) 195–217, https://doi.org/10.5194/essd-10-195-2018.
- [4] U.S. Geological Survey, "Mineral Commodity Summaries," 2020. [Online]. Available: https://doi.org/10.3133/mcs2020.
- [5] IEA, "Technology Roadmap Low-Carbon Transition in the Cement Industry," Paris, 2018. [Online]. Available: https://www.iea.org/reports/technology-roadmap-low-carbon-transition-in-the-cement-industry.
- [6] R.J. Flatt, N. Roussel, C.R. Cheeseman, Concrete: An eco material that needs to be improved, J. Eur. Ceram. Soc. 32 (11) (Aug. 2012) 2787–2798, https://doi.org/ 10.1016/j.jeurceramsoc.2011.11.012.
- [7] S. Mindess, D. Darwin, J.F. Young, Concrete, 2nd ed., Pearson Education Inc, Upper Saddle River, NJ, 2003.
- [8] J.L. Provis, J.S.J. van Deventer, Alkali Activated Materials, vol. 13, Springer, Netherlands, Dordrecht, 2014.
- [9] J.L. Provis, Alkali-activated materials, Cem. Concr. Res. 114 (Dec. 2018) 40–48, https://doi.org/10.1016/j.cemconres.2017.02.009.
- [10] Y. Dhandapani, T. Sakthivel, M. Santhanam, R. Gettu, R.G. Pillai, Mechanical properties and durability performance of concretes with Limestone Calcined Clay Cement (LC3), Cem. Concr. Res. 107 (May 2018) 136–151, https://doi.org/ 10.1016/j.cem.conres.2018.02.005.
- [11] H. Justnes, T.A. Østnor, "Alternative Binders Based on Lime and Calcined Clay", in Calcined Clays for Sustainable, Concrete (2015) 51–57, https://doi.org/10.1007/ 978-04-017-0939-3-7
- [12] A.J.W. Harrison, "Reactive magnesium oxide cements," U.S. Patent No. 7,347,896, 2008.
- [13] A. Al-Tabbaa, "Reactive magnesia cement," in Eco-Efficient Concrete, Elsevier, 2013, pp. 523–543.
- [14] S.A. Walling, J.L. Provis, Magnesia-based cements: a journey of 150 years, and cements for the future? Chem. Rev. 116 (7) (2016) 4170–4204, https://doi.org/ 10.1021/acs.chemrev.5b00463.
- [15] C. Du, A review of magnesium oxide in concrete, Concr. Int. 27 (12) (2005) 45–50.

- [16] N.T. Dung, C. Unluer, Sequestration of CO 2 in reactive MgO cement-based mixes with enhanced hydration mechanisms, Constr. Build. Mater. 143 (Jul. 2017) 71–82, https://doi.org/10.1016/j.conbuildmat.2017.03.038.
- [17] N.T. Dung, C. Unluer, Improving the performance of reactive MgO cement-based concrete mixes, Constr. Build. Mater. 126 (2016) 747–758, https://doi.org/ 10.1016/j.conbuildmat.2016.09.090.
- [18] R.J.M. Wolfs, F.P. Bos, T.A.M. Salet, Early age mechanical behaviour of 3D printed concrete: Numerical modelling and experimental testing, Cem. Concr. Res. 106 (2018) 103–116, https://doi.org/10.1016/j.cemconres.2018.02.001.
- [19] F. Bos, R. Wolfs, Z. Ahmed, T. Salet, Additive manufacturing of concrete in construction: potentials and challenges of 3D concrete printing, Virtual Phys. Prototyp. 11 (3) (2016) 209–225, https://doi.org/10.1080/ 17452759.2016.1209867.
- [20] R. Duballet, C. Gosselin, P. Roux, "Additive Manufacturing and Multi-Objective Optimization of Graded Polystyrene Aggregate Concrete Structures," in Modelling Behaviour, Cham: Springer International Publishing, 2015, pp. 225–235.
- [21] Z.Y. Ahmed, F.P. Bos, R.J.M. Wolfs, T. Salet, "Design considerations due to scale effects in 3d concrete printing," in 8th International Conference of the Arab Society for Computer Aided Architectural Design, 2016, pp. 1–10, Accessed: Apr. 29, 2021. [Online]. Available: https://research.tue.nl/en/publications/design-consideration s-due-to-scale-effects-in-3d-concrete-printin.
- [22] T.T. Le, S.A. Austin, S. Lim, R.A. Buswell, A.G.F. Gibb, T. Thorpe, Mix design and fresh properties for high-performance printing concrete, Mater. Struct. 45 (8) (Aug. 2012) 1221–1232, https://doi.org/10.1617/s11527-012-9828-z.
- [23] B. Panda, S.C. Paul, N.A.N. Mohamed, Y.W.D. Tay, M.J. Tan, Measurement of tensile bond strength of 3D printed geopolymer mortar, Measurement 113 (2018) 108–116, https://doi.org/10.1016/j.measurement.2017.08.051.
- [24] R.J.M. Wolfs, F.P. Bos, T.A.M. Salet, Hardened properties of 3D printed concrete: The influence of process parameters on interlayer adhesion, Cem. Concr. Res. 119 (February) (2019) 132–140, https://doi.org/10.1016/j.cemconres.2019.02.017.
- [25] F. Bos, R. Wolfs, Z. Ahmed, T. Salet, Additive manufacturing of concrete in construction: potentials and challenges of 3D concrete printing, Virtual Phys. Prototyp. 11 (3) (2016) 209–225, https://doi.org/10.1080/ 17452759.2016.1209867.
- [26] R.A. Buswell, W.R. Leal de Silva, S.Z. Jones, J. Dirrenberger, 3D printing using concrete extrusion: A roadmap for research, Cem. Concr. Res. 112 (2018) 37–49, https://doi.org/10.1016/j.cemconres.2018.05.006.
- [27] N. Labonnote, A. Rønnquist, B. Manum, P. Rüther, Additive construction: State-of-the-art, challenges and opportunities, Autom. Constr. 72 (Dec. 2016) 347–366, https://doi.org/10.1016/j.autcon.2016.08.026.
- [28] G. De Schutter, K. Lesage, V. Mechtcherine, V.N. Nerella, G. Habert, I. Agusti-Juan, Vision of 3D printing with concrete — Technical, economic and environmental potentials, Cem. Concr. Res. 112 (Oct. 2018) 25–36, https://doi.org/10.1016/j. cemconres.2018.06.001.
- [29] N. Roussel, Rheological requirements for printable concretes, Cem. Concr. Res. 112 (2018) 76–85, https://doi.org/10.1016/j.cemconres.2018.04.005.
- [30] S.C. Paul, G.P.A.G. van Zijl, M.J. Tan, I. Gibson, A review of 3D concrete printing systems and materials properties: current status and future research prospects, Rapid Prototyp. J. 24 (4) (2018) 784–798, https://doi.org/10.1108/RPJ-09-2016-0154.
- [31] T. Wangler, N. Roussel, F.P. Bos, T.A.M. Salet, R.J. Flatt, Digital concrete: a review, Cem. Concr. Res. 123 (2019), 105780, https://doi.org/10.1016/j. cemconres.2019.105780.
- [32] B. Lu, Y. Weng, M. Li, Y.e. Qian, K.F. Leong, M.J. Tan, S. Qian, A systematical review of 3D printable cementitious materials, Constr. Build. Mater. 207 (2019) 477–490, https://doi.org/10.1016/j.conbuildmat.2019.02.144.
- [33] G. Ma, Z. Li, L. Wang, F. Wang, J. Sanjayan, Mechanical anisotropy of aligned fiber reinforced composite for extrusion-based 3D printing, Constr. Build. Mater. 202 (2019) 770–783, https://doi.org/10.1016/j.conbuildmat.2019.01.008.
- [34] D. Heras Murcia, M. Genedy, M.M. Reda Taha, Examining the significance of infill printing pattern on the anisotropy of 3D printed concrete, Constr. Build. Mater. 262 (2020), 120559, https://doi.org/10.1016/j.conbuildmat.2020.120559.
- [35] B. Zareiyan, B. Khoshnevis, Interlayer adhesion and strength of structures in Contour Crafting - Effects of aggregate size, extrusion rate, and layer thickness, Autom. Constr. 81 (2017) 112–121, https://doi.org/10.1016/j. autcon.2017.06.013.
- [36] B. Panda, S. Chandra Paul, M. Jen Tan, Anisotropic mechanical performance of 3D printed fiber reinforced sustainable construction material, Materials Letters 209 (2017) 146–149.
- [37] P. Feng, X. Meng, J.-F. Chen, L. Ye, Mechanical properties of structures 3D printed with cementitious powders, Constr. Build. Mater. 93 (2015) 486–497, https://doi. org/10.1016/j.conbuildmat.2015.05.132.
- [38] V.N. Nerella, V. Mechtcherine, "Studying the Printability of Fresh Concrete for Formwork-Free Concrete Onsite 3D Printing Technology (CONPrint3D)," in 3D Concrete Printing Technology, Elsevier, 2019, pp. 333–347.
- [39] Y. Chen, C. Romero Rodriguez, Z. Li, B. Chen, O. Çopuroğlu, and E. Schlangen, "Effect of different grade levels of calcined clays on fresh and hardened properties of ternary-blended cementitious materials for 3D printing," Cem. Concr. Compos., vol. 114, p. 103708, Nov. 2020, 10.1016/j.cemconcomp.2020.103708.
- [40] A. Khalil, X. Wang, K. Celik, 3D printable magnesium oxide concrete: towards sustainable modern architecture, Addit. Manuf. 33 (2020), 101145, https://doi. org/10.1016/j.addma.2020.101145.
- [41] S.C. Paul, Y.W.D. Tay, B. Panda, M.J. Tan, Fresh and hardened properties of 3D printable cementitious materials for building and construction, Arch. Civ. Mech. Eng. 18 (1) (2018) 311–319, https://doi.org/10.1016/j.acme.2017.02.008.

- [42] R.W. and T.S.Z. Ahmed, F. Bos, "Design considerations due to scale effects in 3D concrete printing," in: Proceedings of 8th International Conference of the Arab Society for Computer Aided Architectural Design (ASCAAD 2016), 2016, pp. 1–10.
- [43] A.V. Rahul, M. Santhanam, H. Meena, Z. Ghani, 3D printable concrete: Mixture design and test methods, Cem. Concr. Compos. 97 (2019) 13–23, https://doi.org/ 10.1016/j.cemconcomp.2018.12.014.
- [44] A. Kazemian, X. Yuan, E. Cochran, B. Khoshnevis, Cementitious materials for construction-scale 3D printing: Laboratory testing of fresh printing mixture, Constr. Build. Mater. 145 (2017) 639–647, https://doi.org/10.1016/j. conbuildmat.2017.04.015.
- [45] O.A. Mendoza Reales, P. Duda, E.C.C.M. Silva, M.D.M. Paiva, R.D.T. Filho, Nanosilica particles as structural buildup agents for 3D printing with Portland cement pastes, Constr. Build. Mater. 219 (2019) 91–100.
- [46] M. Charrier, C. Ouellet-Plamondon, Testing Procedures on Materials to Formulate the Ink for 3D Printing, Transp. Res. Rec. J. Transp. Res. Board 2674 (2) (Feb. 2020) 21–32, https://doi.org/10.1177/0361198120907583.
- [47] J.G. Sanjayan, B. Nematollahi, M. Xia, T. Marchment, Effect of surface moisture on inter-layer strength of 3D printed concrete, Constr. Build. Mater. 172 (May 2018) 468–475, https://doi.org/10.1016/j.conbuildmat.2018.03.232.
- [48] K.P. Matabola, E.M. van der Merwe, C.A. Strydom, F.J.W. Labuschagne, The influence of hydrating agents on the hydration of industrial magnesium oxide, J. Chem. Technol. Biotechnol. 85 (12) (Dec. 2010) 1569–1574, https://doi.org/ 10.1002/ictb.2467.
- [49] D. Filippou, N. Katiforis, N. Papassiopi, K. Adam, On the kinetics of magnesia hydration in magnesium acetate solutions, J. Chem. Technol. Biotechnol. 74 (4) (1991) 322–328
- [50] C. Unluer, A. Al-Tabbaa, The role of brucite, ground granulated blastfurnace slag, and magnesium silicates in the carbonation and performance of MgO cements, Constr. Build. Mater. 94 (2015) 629–643, https://doi.org/10.1016/j. conbuildmat.2015.07.105.
- [51] R. Zhang, "Carbonated Reactive MgO-Portland Cement Blends: Chemistry, Microstructure and Properties," 2018.
- [52] Y. Qian, S. Kawashima, Use of creep recovery protocol to measure static yield stress and structural rebuilding of fresh cement pastes, Cem. Concr. Res. 90 (2016) 73–79, https://doi.org/10.1016/j.cemconres.2016.09.005.
- [53] B. Panda, S. Ruan, C. Unluer, M.J. Tan, Improving the 3D printability of high volume fly ash mixtures via the use of nano attapulgite clay, Compos. Part B Eng. 165 (2019) 75–83, https://doi.org/10.1016/j.compositesb.2018.11.109.
- [54] B. Panda, C. Unluer, M.J. Tan, Extrusion and rheology characterization of geopolymer nanocomposites used in 3D printing, Compos. Part B Eng. 176 (2019), 107290, https://doi.org/10.1016/j.compositesb.2019.107290.
- [55] M.A. Moeini, M. Hosseinpoor, A. Yahia, Effectiveness of the rheometric methods to evaluate the build-up of cementitious mortars used for 3D printing, Constr. Build. Mater. 257 (2020), 119551, https://doi.org/10.1016/j.conbuildmat.2020.119551.
- [56] S. Ma, S. Kawashima, A rheological approach to study the early-age hydration of oil well cement: Effect of temperature, pressure and nanoclay, Constr. Build. Mater. 215 (2019) 119–127, https://doi.org/10.1016/j.conbuildmat.2019.04.177.
- [57] Y. Qian, S. Ma, S. Kawashima, G. De Schutter, Rheological characterization of the viscoelastic solid-like properties of fresh cement pastes with nanoclay addition, Theor. Appl. Fract. Mech. 103 (2019), 102262, https://doi.org/10.1016/j. tafmec.2019.102262.
- [58] S. Ma, Y. Qian, S. Kawashima, Experimental and modeling study on the non-linear structural build-up of fresh cement pastes incorporating viscosity modifying admixtures, Cem. Concr. Res. 108 (2018) 1–9, https://doi.org/10.1016/j. cemeonres 2018 02 022
- [59] A. Douba, S. Ma, S. Kawashima, Rheology of fresh cement pastes modified with nanoclay-coated cements, Cem. Concr. Compos. 125 (2022) 104301, https://doi. org/10.1016/j.cemconcomp.2021.104301.
- [60] A. D. and S. Kawashima, "Use of Nanoclays and Methylcellulose to Tailor Rheology for Three-Dimensional Concrete Printing," ACI Mater. J., vol. 118, no. 6, 10.14359/ 51733129
- [61] T.-P. Chang, J.-Y. Shih, K.-M. Yang, T.-C. Hsiao, Material properties of portland cement paste with nano-montmorillonite, J. Mater. Sci. 42 (17) (2007) 7478–7487, https://doi.org/10.1007/s10853-006-1462-0.

- [62] K. Kovler, N. Roussel, Properties of fresh and hardened concrete, Cem. Concr. Res. 41 (7) (2011) 775–792, https://doi.org/10.1016/j.cemconres.2011.03.009.
- [63] Y. Liu, J. Han, M. Li, P. Yan, Effect of a nanoscale viscosity modifier on rheological properties of cement pastes and mechanical properties of mortars, Constr. Build. Mater. 190 (2018) 255–264, https://doi.org/10.1016/j.conbuildmat.2018.09.110.
- [64] N. Roussel, Rheological requirements for printable concretes, Cem. Concr. Res. 112 (2018) 76–85, https://doi.org/10.1016/j.cemconres.2018.04.005.
- [65] P. Bhardwaj, M. Kamil, M. Panda, Surfactant-polymer interaction: effect of hydroxypropylmethyl cellulose on the surface and solution properties of gemini surfactants, Colloid Polym. Sci. 296 (11) (2018) 1879–1889, https://doi.org/ 10.1007/s00396-018-4409-5
- [66] J.Y. Zhang, X.P. Wang, H.Y. Liu, J.A. Tang, L. Jiang, Interfacial rheology investigation of polyacrylamide-surfactant interactions, Colloids Surfaces A Physicochem. Eng. Asp. 132 (1) (1998) 9–16, https://doi.org/10.1016/S0927-7757(97)00151-9
- [67] S. Ma, S. Kawashima, Investigating the working mechanisms of viscosity-modifying admixtures through rheological and water transport properties, J. Mater. Civ. Eng. 32 (2) (2020) 04019357, https://doi.org/10.1061/(ASCE)MT.1943-5533.0003018.
- [68] C. Brumaud, R. Baumann, M. Schmitz, M. Radler, N. Roussel, Cellulose ethers and yield stress of cement pastes, Cem. Concr. Res. 55 (2014) 14–21, https://doi.org/ 10.1016/j.cemconres.2013.06.013.
- [69] L. Patural, P. Marchal, A. Govin, P. Grosseau, B. Ruot, O. Devès, Cellulose ethers influence on water retention and consistency in cement-based mortars, Cem. Concr. Res. 41 (1) (2011) 46–55, https://doi.org/10.1016/j. cemconres.2010.09.004.
- [70] A. Mohammed, N.T.K. Al-Saadi, Ultra-high early strength cementitious grout suitable for additive manufacturing applications fabricated by using graphene oxide and viscosity modifying agents, Polymers (Basel) 12 (12) (Dec. 2020) 2900, https://doi.org/10.3390/polym12122900.
- [71] M. Sonebi, A. Perrot, Effect of mix proportions on rheology and permeability of cement grouts containing viscosity modifying admixture, Constr. Build. Mater. 212 (2019) 687–697. https://doi.org/10.1016/j.conbuildmat.2019.04.022.
- [72] S. Chaves Figueiredo, O. Çopuroğlu, E. Schlangen, Effect of viscosity modifier admixture on Portland cement paste hydration and microstructure, Constr. Build. Mater. 212 (2019) 818–840.
- [73] S. Ma, A.H. Akca, D. Esposito, S. Kawashima, Influence of aqueous carbonate species on hydration and carbonation of reactive MgO cement, J. CO2 Util. 41 (2020) Oct, https://doi.org/10.1016/j.jcou.2020.101260.
- [74] L. Pu, C. Unluer, Investigation of carbonation depth and its influence on the performance and microstructure of MgO cement and PC mixes, Constr. Build.
- Mater. 120 (2016) 349–363, https://doi.org/10.1016/j.conbuildmat.2016.05.067.

  [75] W.A. John, A.B. Richard, C.N. Monte, Handbook of Mineralogy, Mineralogical
- Society of America, Chantilly, 2001.
  [76] L.J. Vandeperre, A. Al-Tabbaa, Accelerated carbonation of reactive MgO cements, Adv. Cem. Res. 19 (2) (2007) 67–79, https://doi.org/10.1680/adcr.2007.19.2.67.
- [77] D. N. T. and U. C., "Improving the Carbonation of Reactive MgO Cement Concrete via the Use of NaHCO3 and NaCl," J. Mater. Civ. Eng., vol. 30, no. 12, p. 4018320, Dec. 2018, 10.1061/(ASCE)MT.1943-5533.0002509.
- [78] L. Pu, C. Unluer, Investigation of carbonation depth and its influence on the performance and microstructure of MgO cement and PC mixes, Constr. Build. Mater. 120 (2016) 349–363, https://doi.org/10.1016/j.conbuildmat.2016.05.067.
- [79] G. Jauffret, J. Morrison, F.P. Glasser, On the thermal decomposition of nesquehonite, J. Therm. Anal. Calorim. 122 (2) (2015) 601–609, https://doi.org/10.1007/s10973-015-4756-0
- [80] R.M. Dell, S.W. Weller, The thermal decomposition of nesquehonite MgCO3  $\cdot$  3H 2O and magnesium ammonium carbonate MgCO3  $\cdot$  (NH4)2CO3  $\cdot$  4H2O, Trans. Faraday Soc. 55 (1959) 2203–2220, https://doi.org/10.1039/TF9595502203.
- [81] H. Ren, et al., Thermal characterization and kinetic analysis of nesquehonite, hydromagnesite, and brucite, using TG-DTG and DSC techniques, J. Therm. Anal. Calorim. 115 (2) (2014) 1949–1960, https://doi.org/10.1007/s10973-013-3372-
- [82] S. Ma, A.H. Akca, D. Esposito, S. Kawashima, Influence of aqueous carbonate species on hydration and carbonation of reactive MgO cement, J. CO2 Util. 41 (2020) 101260, https://doi.org/10.1016/j.jcou.2020.101260.